Tellus SERIES B CHEMICAL AND PHYSICAL METEOROLOGY
PUBLISHED BY THE INTERNATIONAL METEOROLOGICAL INSTITUTE IN STOCKHOLM

Tellus (2011), 63B, 549–572
Printed in Singapore. All rights reserved

TELLUS

In situ aerosol characterization at Cape Verde

Part 2: Parametrization of relative humidity- and wavelength-dependent aerosol optical properties

By ALEXANDER SCHLADITZ[1]*, THOMAS MÜLLER[1], STEPHAN NORDMANN[1], MATTHIAS TESCHE[1], SILKE GROß[2], VOLKER FREUDENTHALER[2], JOSEF GASTEIGER[2] and ALFRED WIEDENSOHLER[1], [1]*Leibniz Institute for Tropospheric Research (IfT), Permoserstraße 15, 04318 Leipzig, Germany*; [2]*Meteorological Institute, Ludwig–Maximilians–Universität, Theresienstraße 37, 80333 Munich, Germany*

(Manuscript received 8 December 2010; in final form 7 June 2011)

ABSTRACT

An observation-based numerical study of humidity-dependent aerosol optical properties of mixed marine and Saharan mineral dust aerosol is presented. An aerosol model was developed based on measured optical and microphysical properties to describe the marine and Saharan dust aerosol at Cape Verde. A wavelength-dependent optical equivalent imaginary part of the refractive index and a scattering non-sphericity factor for Saharan dust were derived. Simulations of humidity effects on optical properties by the aerosol model were validated with relative measurements of the extinction coefficient at ambient conditions. Parametrizations were derived to describe the humidity dependence of the extinction, scattering, and absorption coefficients as well as the asymmetry parameter and single scattering albedo. For wavelengths (300–950 nm) and dry dust volume fractions (0–1), aerosol optical properties as a function of relative humidity (RH = 0–90%) can be calculated from tabulated parameters. For instance, at a wavelength of 550 nm, a volume fraction of 0.5 of dust on the total particle volume (dry conditions) and a RH of 90%, the enhancements for the scattering, extinction and absorption coefficients are 2.55, 2.46 and 1.04, respectively, while the enhancements for the asymmetry parameter and single scattering albedo are 1.11 and 1.04.

1. Introduction

Atmospheric aerosol particles play an important role for the radiative budget of the Earth's atmosphere. The aerosol radiative forcing (RF), which is directly related to the global mean equilibrium temperature at the Earth's surface (Ramaswamy et al., 2001), can be categorized into the direct and the indirect effect. The direct effect alters the radiative balance of the Earth's atmosphere by scattering and absorbing short-wave solar and long-wave terrestrial radiation. Numerous research studies (e.g. Forster et al., 2007 and references therein) revealed positive and negative contributions to the direct RF by, for example, anthropogenic haze, biomass burning, mineral dust from desert regions and marine (sulphate and sea-salt) aerosol particles. The recent IPCC report (IPCC, 2007) rates the scientific understanding of the direct RF to be medium or even low.

Crucial parameters to quantify the direct RF are the surface albedo (dark or bright surface), the cloudiness, the vertical aerosol distribution, aerosol optical depth and wavelength-dependent aerosol optical properties (complex refractive index, asymmetry parameter and single scattering albedo; Seinfeld and Pandis, 2006; Tegen et al., 1996). The aerosol optical properties (AOPs) may also depend significantly on the relative humidity (RH; Kasten, 1969; Covert et al., 1972; Hänel, 1976). An explicit calculation of AOPs at ambient conditions by using the Köhler theory (Köhler, 1936) tends to be too complex to be applicable in a global circulation model including radiative transfer calculations. Empirical growth laws determined from experimental data may therefore provide a more applicable solution to better approximate ambient aerosol radiative properties in global circulation models.

The humidity dependence of the scattering coefficient of the marine aerosol was determined from experimental data for several locations of the world, for example, off the pacific coast of the United States (Hegg et al., 1996), in the Pacific and Southern Oceans (Carrico et al., 1998) and in the northern Atlantic

*Corresponding author.
e-mail: alexander.schladitz@tropos.de
DOI: 10.1111/j.1600-0889.2011.00568.x

during ACE-2 (Carrico et al., 2000; Gassó et al., 2000). Humidity dependence on AOPs in the presence of Asian dust during ACE–Asia was reported by Anderson et al. (2003), Carrico et al. (2003), Howell et al. (2006) and Yoon and Kim (2006). RH-dependent AOPs of a mixture of marine and transported Saharan dust aerosol were published by Li-Jones et al. (1998) and Lack et al. (2009). The weakness of most of the publications given above is to present the humidity dependence for only one AOP (e.g. absorption or scattering coefficients) for few wavelengths (530, 532 and 550 nm).

In contrast, the amenity of aerosol models (e.g. Hänel, 1976; Shettle and Fenn, 1979; D'Almeida et al., 1991; Hess et al., 1998) is that they deliver a comprehensive set of humidity dependent AOPs for certain aerosol species for a large wavelength range. In some regions, the aerosol consists however, of a mixture of aerosol species, for example, mineral dust and marine aerosol. The aerosol model by Hess et al. (1998) allows the calculation of AOPs for aerosol mixtures at defined RH. However, the aforementioned models are based on the assumption of spherical particles. To conclude, a comprehensive quantification of humidity effects on AOPs of an aerosol mixture, which also treats the non-sphericity of particles, is presently a gap in knowledge.

To fill this gap, this paper provides model calculations of the humidity dependence on AOPs of a mixture of Saharan dust and marine aerosol, which are the two major natural aerosol species worldwide (Andreae, 1995). The model is based on measurements made in the Cape Verde region in winter 2008, when dust plumes from the Saharan desert spread over the Atlantics (Chiapello et al., 1997). One calculated property by the model, for example, the humidity effect on the extinction coefficient at ambient conditions, is verified by an independent relative measurement. Beyond that, this investigation presents parametrizations of AOPs as function of the RH, dust fraction (dry conditions) and wavelength of the incident radiation.

The results of the model calculations as well as the parametrizations can be either used for radiative transfer models or to predict the AOPs in the lowest levels of the atmospheric boundary layer. The latter point will be important to extend measured extinction profiles from lidar systems to the ground. With this complete extinction profile, the aerosol optical depth can be calculated and compared with data from sun-photometry.

2. Location and measurement conditions

The measurements were conducted from January 17 to February 10, 2008 (day of year, DOY 17.0–42.0) in the framework of the Saharan mineral dust experiment part 2 (SAMUM-2, Ansmann et al., 2011). As shown in Fig. 1, the measurement site was located northeast from the capital Praia (14°57′N, 23°29′W, 101 m height above sea level, asl) on the Island of Santiago, Cape Verde. The measurements took place on a small rise on the north end of the runway of Praia airport, 2 km away from the coastline.

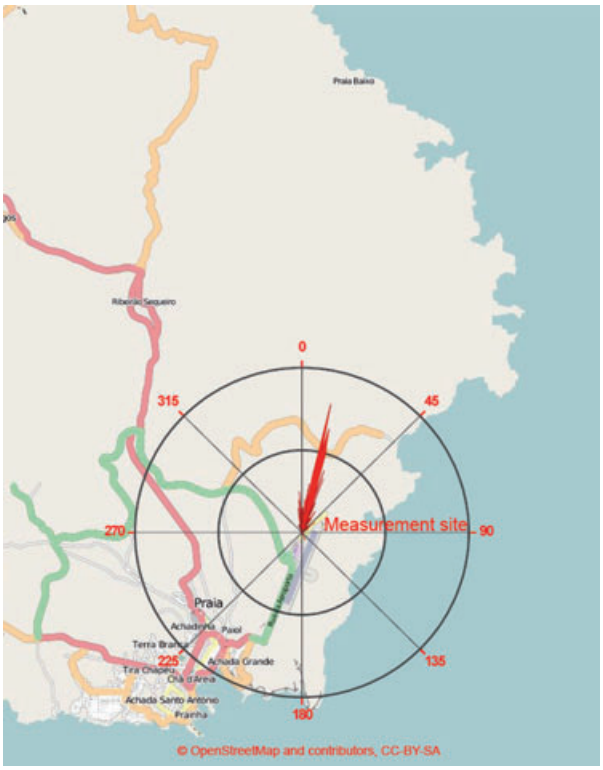

Fig. 1. Map of the southeastern part of Santiago Island, Cape Verde taken from OpenStreetMap (http://www.openstreetmap.org/) under license CC-BY-SA (http://creativecommons.org/licenses/by-sa/2.0/). A wind rose was plotted into the map, which shows the relative frequency of the wind direction at the measurement site. The position of the measurement site is labelled by the centre of the wind rose.

To determine if values measured at the station are representative and not be affected by local aerosol sources, the measured wind direction at the site was analysed. A wind rose, showing the relative frequency of the wind direction at the measurement site, is added to Fig. 1. Due to the influence of the trade wind, the predominant wind flow was from north–northeast to northeast and therefore urban contamination from the island can be excluded.

Measurements of the scattering and the absorption coefficient were performed at dry conditions inside a measurement container. An aerosol PM_{10} inlet (Rupprecht and Patashnik Co. Inc., Albany, NY, USA) at about 6 m height above ground was employed to remove particles larger than 10 μm aerodynamic diameter ($dp_a < 10$ μm). To achieve an optimal size cut, a flow rate of 16.7 l min^{-1} is required. Downstream of the aerosol inlet, an automatic aerosol diffusion dryer (Tuch et al., 2009) was used to dry the sample aerosol below 30% RH. The aerosol dryer was installed vertically to avoid gravitational losses of the particles in the sampling line. Downstream of the dryer and inside of the container, the sample aerosol was isokinetically split to conduct the aerosol to the instruments. The mean air temperature inside the container was kept constant (293 ± 2 K).

In contrast to particulate scattering and absorption, the 'extinction coefficient' (inverse to atmospheric visibility) of the aerosol was measured at ambient RH 1.5 m above the container roof at about 5 m height above ground. Ambient temperature and RH were measured at the same height by a Humicap sensor (HMP233, Vaisala, Vantaa, Finland). Air pressure was measured at station level with a barometric sensor (type 5002, Friedrichs, Schenefeld, Germany).

3. Instrumentation and basic corrections

Measurements needed for the aerosol model development including the dry particle number size distribution (PNSD), the hygroscopic growth factor and the hygroscopic state of mixing are taken from Schladitz et al. (2011). Here, we briefly introduce the different measurement techniques for AOPs. Beyond that, an overview of calibrations and measurement uncertainties are given.

3.1. Ambient extinction coefficient

The extinction coefficient of the ambient aerosol was measured by a visibility sensor (VPF 710, Biral, Bristol, UK). The visibility sensor detects the scattered light within a small scattering angle range of $45 \pm 6^{\circ}$ and operates at a wavelength of 880 nm. An internal stored calibration constant, which is unfortunately unknown, converts the measured scattered signal into an extinction coefficient. Therefore, the visibility sensor is used here as a relative measurement of the extinction coefficient. Contaminations of the windows in front of the receiver and transmitter unit influence the measured signal. Therefore, these windows were daily cleaned and the measured signal was checked with a calibration standard. The relative uncertainty of the visibility sensor given in the user manual decreases with decreasing atmospheric extinction (increasing visibility) and is smaller than 10% for $\sigma_e > 187\,\mathrm{Mm}^{-1}$ and smaller than 20% for $\sigma_e > 100\,\mathrm{Mm}^{-1}$. The manufacturer gives however no uncertainty for $\sigma_e < 100\,\mathrm{Mm}^{-1}$. Therefore, a relative uncertainty of 20% was assumed.

3.2. Scattering coefficient

Integrating nephelometer (Model 3563, Serial no. 1027, TSI Inc., St. Paul, MN, USA) determine a quantity that is close to the particulate scattering and hemispheric backscattering coefficient at three wavelengths $\lambda = 450$, 550 and 700 nm. The setup and the function of the instrument are described in detail by Anderson et al. (1996) and Heintzenberg et al. (2006). The sample aerosol is drawn through an inlet via a blower or an external vacuum supply. During the campaign, the blower was removed and bypassed, and the nephelometer was placed upstream the multiangle absorption photometer (MAAP) that operates with an external vacuum pump (see Fig. 2). The advantage of this method is to reduce the sample flow through the PM_{10} inlet. In a laboratory experiment before the measurement campaign it was checked that no particle losses occur inside the nephelometer. Automatic zero measurements with particle-free air were performed daily to correct the scattering coefficient for wall scattering artifacts due to contamination of the sensing volume. Calibrations with particle-free air and carbon dioxide were carried out before and after the field campaign. The calibration constants deviate within 2% and hence no nephelometer drift during the measurement period was observed. However, the ratio of hemispheric backward to total scattered light was significantly lower than the expected value of 0.5 for a gas molecule. The nephelometer was disassembled and it was found that the backscatter shutter, which shadows the forward scattered light, was deformed such that it blocked some light in the backward direction. As a consequence, data of the hemispheric backscattering coefficient were disregarded for further analysis. The measured (total) scattering coefficient was unaffected.

The measurement uncertainty of the integrating nephelometer was investigated in an intercomparison workshop. Heintzenberg et al. (2006) investigated nine TSI nephelometer (model 3563) using submicrometer and supermicrometer test aerosols. For the submicrometer and the supermicrometer particles, the TSI nephelometer varied within 6% and 13%, respectively.

Due to truncation artifacts of the sensing volume and for the non-Lambertian illumination from the light source, the measured nephelometer scattering coefficient differs from the true scattering coefficient. Numerous investigations present correction factors for a non-Lambertian illumination (e.g. Anderson and Ogren, 1998; Heintzenberg et al., 2006; Bond et al., 2009; Müller et al., 2009b). In this work, the corrections were not applied to the measured scattering coefficient, because within a closure study the measured nephelometer values were used to verify the calculated nephelometer signal (cf. Section 4.1.1). For further considerations, the scattering coefficient measured by the nephelometer is called nephelometer scattering coefficient.

3.3. Absorption coefficient

The particulate light absorption coefficient was measured by three types of absorption photometers, which are all based on the filter measurement technique. These are the MAAP, the particle soot absorption photometer (PSAP), and the spectral optical absorption photometer (SOAP). For regions with soot as the dominating particulate absorber, the MAAP is a reference instrument for the filter measurement technique. For a period with low dust concentration (Section 4.1.2), an intercomparison of MAAP and SOAP data at the same wavelength shows a slope of 0.93 and a Pearson's correlation coefficient of 0.95. However, for regions with mineral dust as the main particulate absorber, the MAAP is not characterized enough. Absorption coefficients derived by the filter based measurement technique should be corrected for particle scattering effects. This effect is however implemented in the radiative transfer scheme solved by

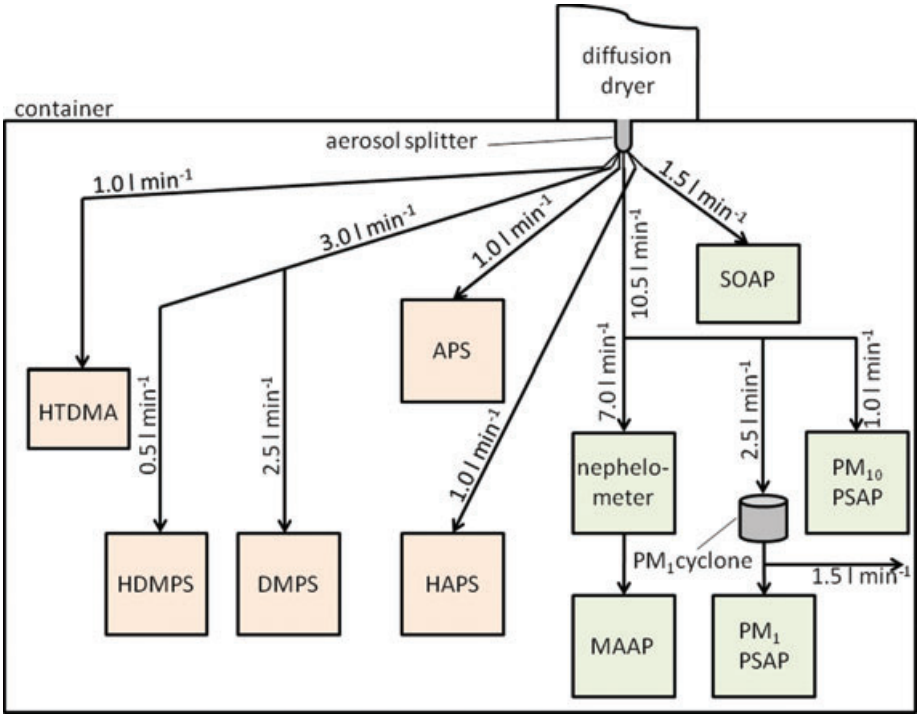

Fig. 2. Instrumental setup of the container and flow rate partitioning to the measurement devices. Instruments for microphysical characterization described in Schladitz et al. (2011) are shown on the left-hand side, whereas optical instrumentation are shown on the right-hand side.

the MAAP, but not sufficiently tested in the presence of mineral dust aerosol with a high single scattering albedo. In this investigation, the data from the MAAP were not used. Therefore, only the PSAP and the SOAP instrument are introduced.

The dry absorption coefficient at $\lambda = 522$ nm (Müller et al., 2010) was determined with two PSAPs (Radiance Research, Seattle, WA, USA). Bond et al. (1999) deliver a detailed description of the PSAP. The flow rates of the PSAPs were calibrated with an electronic bubble flow meter before and after the measurement period and both calibrations differ within 1%. In a laboratory experiment it was tested that the average deviation of the PSAP signals was 6%, which corresponds to the PSAP uncertainty given by Bond et al. (1999).

Following the scheme described in Bond et al. (1999), apparent particulate absorption coefficients derived by both PSAPs were corrected for a scattering artefact using nephelometer scattering coefficients, the deposition spot size of the filter, and the volume flow rate. Nevertheless, Andreae and Gelencsér (2006) pointed out that cross sensitivities of the filter based measurements to the size, single scattering albedo and chemical mixing state cause systematic errors of the absorption coefficient. Bond et al. (1999) proposed that the corrections cannot cover strongly scattering particles (high single scattering albedo) and are insufficient at high filter loadings. Therefore, the absorption coefficient was additionally corrected for filter-loading and particle scattering effects by using a ray-tracing method introduced by Müller et al. (2009a). This method compensates for a loading-dependent sensitivity of the PSAP in cases of high single scattering albedos. The loading effect for purely scattering particles was recently shown in Müller et al. (2010).

The two PSAPs are denoted as PM_{10} PSAP and PM_1 PSAP. The PM_{10} PSAP measured the absorption coefficient behind the PM_{10} inlet, while the PM_1 PSAP was used downstream of an extra sharp cut cyclone (Fig. 2).

The design and the required flow rates of the cyclone are reported in Kenny and Gussman (1997) and Kenny and Gussman (2000). The cyclone efficiency curve at a default volume flow rate of 2.5 l min^{-1} was determined with an Aerodynamic Particle Sizer (APS) during a laboratory experiment, which shows a 50% penetration around $dp_a = 1$ μm (volume equivalent diameter, $dp_{ve} = 701$ nm). A sigmoidal function (cf. Winklmayr et al., 1990) was fitted to the experimental data:

$$f_{PM_1}(dp_{ve}) = -0.0037 + \frac{1.0005 + 0.0037}{1 + \left(\frac{dp_{ve}}{700.75}\right)^{7.0556}}. \quad (1)$$

The SOAP was designed to measure the absorption coefficient in a wavelength range from 300 to 950 nm. In contrast to the PSAP, the transmitted and the reflected light at 140° are detected for blank and particle laden filters. Key components of the SOAP are a deuterium–halogen light source, two optical spectrometers with an optical resolution of 25 nm, and a sensing head, which collects the particle on a filter, to illuminate the sample spot and to measure the transmittance and the reflectance. A radiative

transfer model calculates the absorption coefficient from the measured transmittance and reflectance. A detailed description of the performance and calibration is given in Müller et al. (2009a, 2011). The measurement uncertainty of the SOAP was estimated to 15% by Müller et al. (2009a) during the SAMUM-1 experiment.

3.4. Soot mass concentration

In the early 1970s, Tuinstra and Koenig (1970) found bands of activated graphitic carbon in the Raman spectrum. Rosen et al. (1978) identified the relationship of the amount of absorbing species and the graphitic soot content of the G-Band at the wavenumber 1585 cm^{-1} in the Raman spectrum.

From the present measurements, the mass concentration of graphitic carbon was determined using Raman spectroscopy. Filter probes sampled with the PM_1 PSAP were analysed with a Bruker IFS 55 spectrometer including a FRA-106 Raman module in backscatter configuration. For each filter probe, the Raman spectrometer delivers a characteristic Raman spectrum, which depends of the amount of graphitic carbon on the substrate.

The calibration of the Raman spectrometer that converts the Raman intensity into a mass load in the unit of $\mu g\ cm^{-2}$ was done by Mertes et al. (2004) using synthetic carbon black (Monarch 71, Cabot Corporation, Billerica, MA, USA). Hence, the calibration is valid for the graphitic carbon content in this specific synthetic carbon black. Due to the similar structure of the Raman spectrum of the synthetic carbon black compared to atmospheric soot probes (Mertes et al., 2004), the measured mass load is a soot mass load. Finally, the mass concentration of soot in the unit of $\mu g\ m^{-3}$ was derived from the soot mass load, the area of the filter deposited with particles, and the total air volume sucked through the filter.

The uncertainty of the soot mass concentration is about 10% (Mertes et al., 2004) and includes the uncertainty of the Raman spectrometer, the systematic error from the calibration, uncertainties of the measured deposited area and the total air volume.

3.5. Microphysical particle properties

Measurements of PNSDs and hygroscopic particle properties are described in detail in the first part of this paper (Schladitz et al., 2011). Nevertheless, some key information about that is presented here.

PNSDs were measured by a Differential Mobility Particle Sizer (DMPS) and an APS in the mobility diameter size range from 26 to 800 nm and aerodynamic size range from 0.835 to 10 μm, respectively. Both size distribution measurements were converted to the volume equivalent particle diameter (dp_{ve}), applying the following assumptions.

In the DMPS size range, the particles are assumed to be spherical, and thus the mobility diameter equals the volume equivalent particle diameter. In the APS size range, a dynamical shape factor (particle density) of 1.08 (2160 $kg\ m^{-3}$) for sea-salt particles and 1.25 (2600 $kg\ m^{-3}$) for Saharan mineral dust particles was used to convert aerodynamic to volume equivalent particle diameter. Finally, both PNSDs were combined and the resulting PNSD was fitted by two lognormal size distributions in the fine mode (typical marine double peak, represented by Aitken and accumulation mode) and two lognormal size distributions in the coarse mode. The coarse modes have geometric mean diameters of 780 and 1790 nm (arithmetic mean value) and are composed of hygroscopic sea-salt particles and nearly hydrophobic Saharan mineral dust.

Size resolved hygroscopic particle properties in terms of hygroscopic growth factors (ratio of the particle size at a certain RH to dry state) and number fractions of hygroscopic/nearly hydrophobic particles were measured by a variety of instruments, called HTDMA[1], HDMPS[2] and HAPS[3]. Applying a new data evaluation algorithm presented in Schladitz et al. (2011), these hygroscopic particle properties were determined quasi-continuous in the size range from 26 nm to 10 μm. Hygroscopic growth factors were parametrized with the single hygroscopicity parameter κ introduced by Petters and Kreidenweis (2007). For example, coarse mode sea-salt particles have a κ value (median) of 0.65 and the number fraction is still variable with values from close to zero to 0.7.

3.6. Data processing and particle transport losses

All measurement computers were regularly synchronized with a master PC. Data were recorded at local time (LT = UTC–1h). Corrupted data were removed caused by, for example, power breakdowns, filter changes in the MAAP and PSAP, routine zeroing in the nephelometer and automate column switches of the aerosol diffusion dryer. Since the HDMPS (cf. Schladitz et al., 2011) was the instrument with the lowest temporal resolution of about three hours, all data were averaged after data processing within this time interval to yield a uniform data set ranging from DOY 17.0 to 42.0. All measured data relate to the thermodynamic conditions inside the container ($T = 293 \pm 2$ K, $p_{amb} = 1001 \pm 1.6$ hPa).

Particle losses for larger particles occur due to, for example, sedimentation and impaction and diffusion for ultrafine particles. In this study, the microphysical and optical properties are more dominated by particles in the coarse mode than in the fine and ultrafine size range and diffusion losses were therefore neglected.

Aspiration due to anisoaxial and anisokinetic sampling, impaction through inertia in bends, and sedimentation through gravitation in inlet tubes for laminar and turbulent flows were

[1]Hygroscopicity Tandem Differential Mobility Analyzer
[2]Humidifying Differential Mobility Particle Sizer
[3]Humidified APS

incorporated. Formulas for the transmission efficiencies were taken from Brockmann (1993).

The instrumentation used for a closure study in Section 4.1.2 and an intercomparison study in Section 5 have different positions in relation to the size spectrometers. That implicates different particle losses, which have to be incorporated for the PNSD measurements. Therefore, a short summary of calculated particle losses is given in the respective sections.

4. Aerosol optical characterization at dry conditions

The primary goal of this section is to deliver parameters of an aerosol model, which describes the optical as well as the microphysical properties of the marine and Saharan dust aerosol at dry conditions. In Section 5, the aerosol model is used to calculate microphysical and optical properties at ambient conditions, for example, mass concentration and the humidity effect of the extinction coefficient.

Microphysical parameters of the aerosol model are lognormal size distributions and corresponding dry particle densities, hygroscopicity parameters κ and the hygroscopic mixing state in terms of number fractions of hygroscopic and nearly hydrophobic particles with a temporal resolution of three hours. To describe the optical properties of the marine and the Saharan dust aerosol, information on the wavelength-dependent complex refractive indices is required. Two methods were applied to determine the complex refractive indices.

First, within a closure of optical properties such as scattering and absorption coefficients at dry conditions, calculated optical properties using refractive indices from literature are compared with measured ones. Second, as a consequence from this closure (differences in the spectral behaviour of the absorption coefficient), an optical equivalent imaginary part of mineral dust is retrieved. In contrast to the imaginary part of the refractive index, the optical equivalent imaginary part implicitly includes the shape of the particle. Therefore, optical properties can be calculated applying Mie theory.

4.1. Closure of optical properties at dry conditions

As first assumption, refractive indices from literature were taken to compare Mie calculated dry scattering and absorption coefficients with measurements. Quasi-continuous PNSDs for the Mie calculations are available from DOY 20.875 to 40.125 LT. The Mie calculations were performed for homogeneous spherical scatterers using the Mie code by Bohren and Huffman (1983). The complex refractive index is taken from the OPAC database (Hess et al., 1998). To each lognormal size distribution (fine and coarse modes) and hygroscopic mixing state (hygroscopic, nearly hydrophobic), a wavelength-dependent complex refractive index was addressed (Table A1). For the coarse mode, the complex refractive index for 'sea-salt (0% RH)' was assigned to the hygroscopic particles, while 'mineral' was assigned to the nearly hydrophobic particles. The complex refractive index for the fine mode was calculated by using an internal mixture of 'soot' and 'insoluble' for the nearly hydrophobic particles, and 'soot' and 'water soluble (0% RH)' for the hygroscopic particles (cf. discussion in Schladitz et al., 2011). The average soot fraction in the fine particle modes is 7.7 $\pm$ 3.1 vol%, and was determined as the ratio of soot mass concentration to total mass concentration in the fine particle modes. To calculate the mixed refractive indices, the Maxwell–Garnett relation (Maxwell-Garnett, 1904) was used, which is a two component mixing rule for the complex refractive index.

4.1.1. Closure of the dry scattering coefficient. To calculate the nephelometer scattering σ_s^{neph}, the angular illumination function $I(\theta)$ was considered. The angular illumination function for the TSI nephelometer is taken from Müller et al. (2009b), which confirms former measurements made by Anderson and Ogren (1998). Müller et al. (2009b) show in their fig. 2 that the angular illumination function obviously deviate from an ideal nephelometer, with $I(\theta) = \sin(\theta)$. Figure 3a shows a time series and Fig. 3b shows a scatter plot of measured and calculated nephelometer scattering coefficients. The 'Pearson's correlation coefficient' (r) is 0.99 for the three wavelengths $\lambda = 450$, 550 and 700 nm. Calculated and measured nephelometer scattering coefficients agree well for $\sigma_s^{neph} < 25$ Mm^{-1}. However for $\sigma_s^{neph} >$ 25 Mm^{-1}, the measured values are larger than the calculated. Figure 3c shows a scatter plot of measured and calculated scattering coefficients with $\sigma_s^{neph} > 25$ Mm^{-1}. Linear regression lines were applied to the data and revealed wavelength-dependent slopes of 1.92 at $\lambda = 450$ nm, 1.65 at $\lambda = 550$ nm and 1.35 at $\lambda = 700$ nm. To interpret this behaviour, the dry dust volume fraction vf_{dust} is introduced by

$$vf_{dust} = \frac{V_{hyd}\,(\text{coarse mode})}{V_{tot}}, \tag{2}$$

where V_{tot} is the total particle volume concentration derived from measured PNSD and V_{hyd} (coarse mode) is the hydrophobic volume concentration of coarse mode particles. The error of the dry dust volume fraction is composed of sizing and counting errors of the size spectrometers (DMPS, APS) and uncertainties to determine the number fraction of nearly hydrophobic particles. The latter, however involves the largest error. In Schladitz et al. (2011), the uncertainty for the number fractions for $dp_{ve} >$ 150 nm was quantified to 24%. A variation of the number fraction of nearly hydrophobic particles causes a linear response to the dry dust volume fraction. Thus, the error for the dry dust volume fraction was also estimated to 24%. Figure 4 illustrates the relationship among the dry dust volume fraction, the measured nephelometer scattering coefficient, and the ratio of measured to calculated nephelometer scattering at $\lambda = 450$ nm. Figure 4 revealed that in most of the cases σ_s^{neph} increases with increasing vf_{dust}. The ratio of measured to calculated scattering increases with σ_s^{neph} as well as with vf_{dust}. Only for low

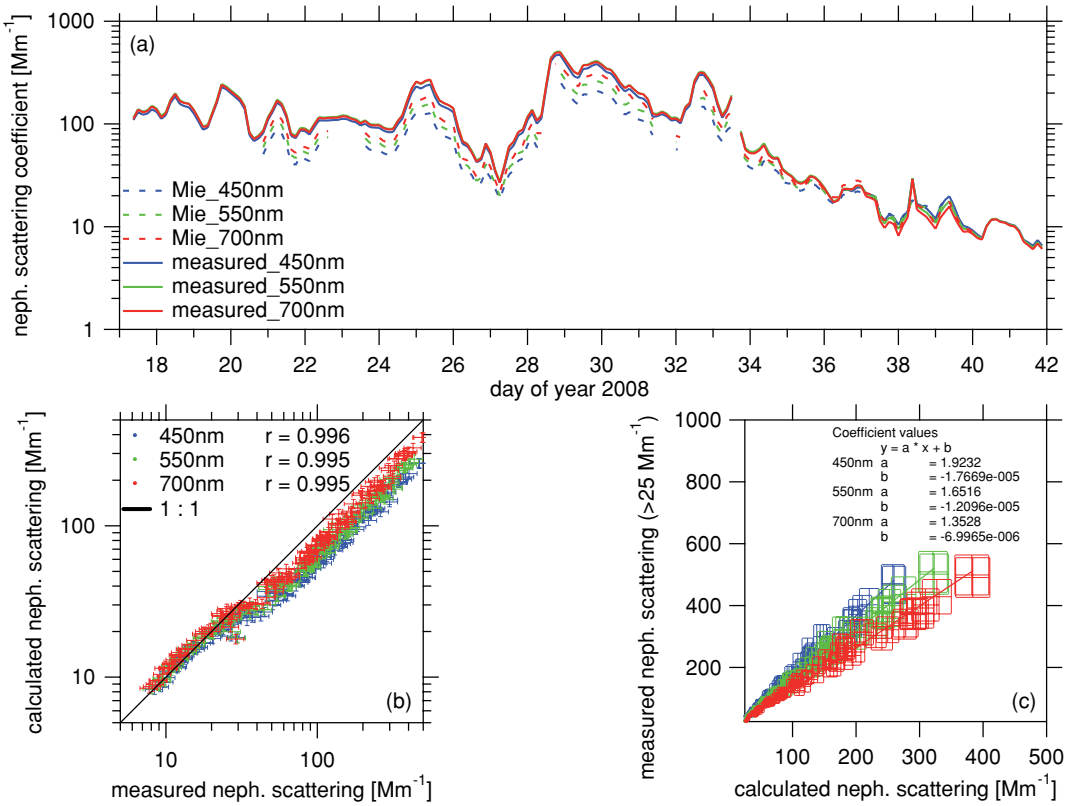

Fig. 3. (a) Time series of Mie calculated and measured nephelometer scattering coefficients at $\lambda = 450$, 550 and 700 nm. (b) Scatter plot of Mie calculated versus measured nephelometer scattering and (c) Scatter plot and linear regression of measured nephelometer scattering >25 Mm^{-1} versus calculated nephelometer scattering. The error for the measured values is given by the nephelometer uncertainty (13%), while the error for the calculated values (single standard deviation) is 7% (Wex et al., 2002).

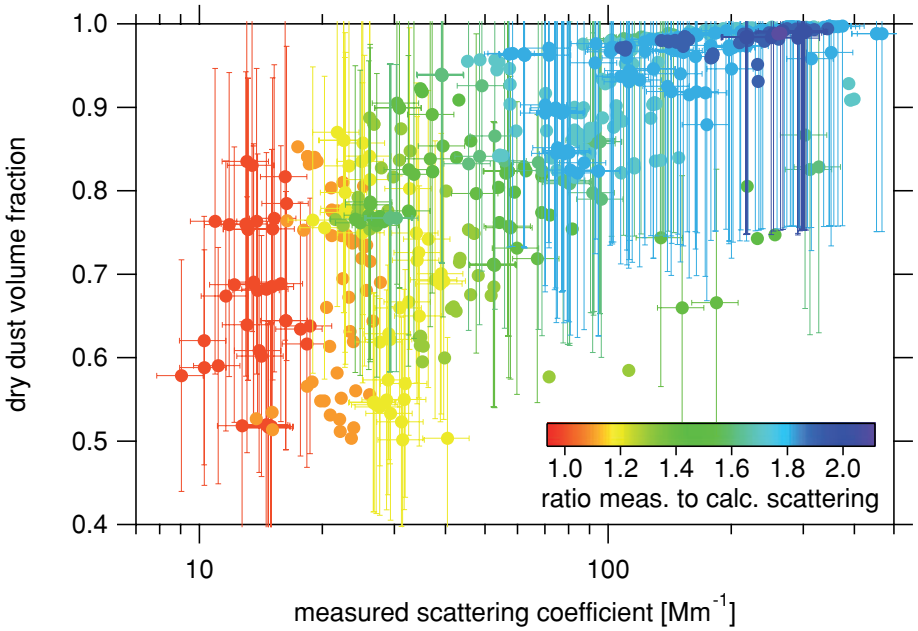

Fig. 4. Relationship between measured scattering coefficient and dry dust volume fraction. The colour indicates the ratio of measured to calculated scattering at $\lambda = 450$ nm. The error for the measured values is given by the nephelometer uncertainty (13%), while the error for the dry dust volume fraction is 24%.

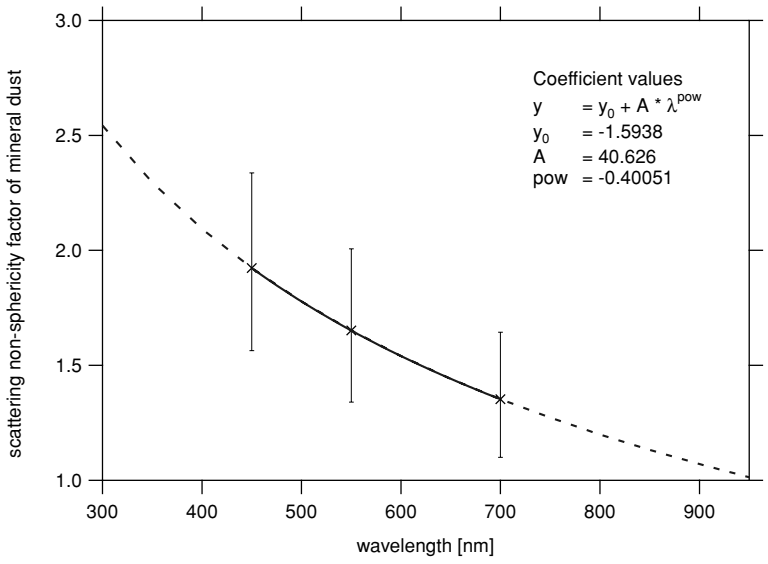

Fig. 5. Average non-sphericity factor for the nephelometer scattering coefficient (black crosses) and fitted power function $y = y_0 + A \cdot \lambda^{pow}$ (grey solid line). Extrapolated power function in the wavelength range from $\lambda = 300$ to 950 nm (grey dashed line). The parameters of the power function are added. The retrieval of the error bars is given in the text.

nephelometer scattering coefficients $\sigma_s^{neph} < 25$ Mm^{-1}, the ratio of measured to calculated nephelometer scattering is independent of vf_{dust}.

Figure 5 illustrates the wavelength-dependent slopes of the linear regression lines (ratios of measured to calculated nephelometer scattering for nephelometer scattering coefficients $\sigma_s^{neph} > 25$ Mm^{-1}) from Fig. 3c. The error for these slopes is calculated as follows. Linear regression lines were fitted for each wavelength to the top left and bottom right corners of the xy-error boxes shown in Fig. 3c. These *xy*-error boxes result from uncertainties of measured and calculated nephelometer scattering, while the latter also considers assumptions of the complex refractive index and counting errors inside size spectrometers. The differences of the slopes calculated with and without the uncertainties of measured and calculated nephelometer scattering, mark the uncertainty of the ratio of measured to calculated nephelometer scattering plotted in Fig. 5. The ratio of measured to calculated nephelometer scattering deviates significantly from unity for all investigated wavelengths. It is concluded, that the deviations of measured and calculated nephelometer scattering coefficients can be explained as a superposition of non-spherical effects by mineral dust particles. The assumption of spherical particles for mineral dust particles underestimates the real scattering coefficient. Therefore, a wavelength-dependent non-sphericity factor for the scattering coefficient of mineral dust is introduced. Additionally, a power function was fitted to the data shown in Fig. 5, in order to extrapolate the non-sphericity factors in the wavelength range from 300 to 950 nm. In order to calculate AOPs, for example, scattering and extinction coefficients as well as the single scattering albedo (Sections 5 and 6), the power function is incorporated in the aerosol model.

These findings are consistency with a similar study in Morocco during SAMUM-1 (Schladitz et al., 2009). Significant deviations of 1.34–1.42 for wavelengths of 637 and 537 nm were observed between measured and Mie calculated scattering coefficients during periods with high dust concentrations.

Section 4.3 gives numerical calculations of non-sphericity effects of mineral dust particles on AOPs. Numerical calculations of the scattering coefficient of modelled non-spherical dust particles cannot 100% reproduce the deviations between measured and Mie calculated nephelometer scattering coefficients of this study.

4.1.2. Closure of the dry absorption coefficient. As done for the scattering coefficients, closure studies were performed for the absorption coefficients, measured by the PM_1 PSAP, PM_{10} PSAP and SOAP. To calculate the absorption coefficient measured with the PM_1 PSAP, the fitted PM_1 penetration curve (eq. 1) was considered. In contrast to the SOAP, both PSAPs were not measuring directly downstream the aerosol inlet (Fig. 2). For this case, particles losses due to aspiration by removal of a lower from a higher flow rate, impaction in bends ($1 \times 90^\circ$, $1 \times 45^\circ$), and sedimentation in horizontal tubes (40 cm in sum) were incorporated in the PSAP calculations. Time series and corresponding scatter plots of measured and calculated absorption coefficients of the PM_1 and PM_{10} PSAP are shown in Fig. 6. In general, the calculations reproduce the measured values with the simple classification of the absorbing species soot and mineral dust into fine and coarse mode. For a more quantitative discussion, the PM_{10} PSAP calculations correlate better ($r = 0.985$) with the measurements than the PM_1 PSAP calculations ($r = 0.455$). The weaker correlation is caused by the assumption of a constant imaginary part of the complex refractive index of the fine mode.

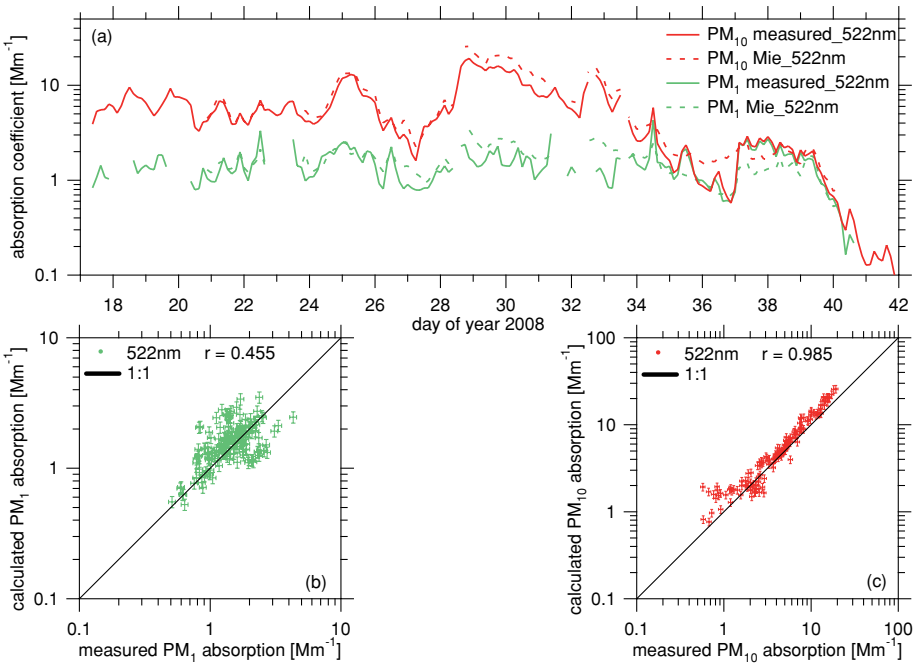

Fig. 6. (a) Time series of Mie calculated and measured absorption coefficients of PM_1 and PM_{10} PSAP at $\lambda = 522$ nm. (b) Scatter plot of calculated and measured absorption coefficients of PM_1 PSAP. (c) Scatter plot of calculated and measured absorption coefficients of PM_{10} PSAP. The error for the measured values is given by the PSAP uncertainty (6%), while the error for the calculated values (single standard deviation) is 10% (Wex et al., 2002).

Figure 7 shows time series and corresponding scatter plots of measured and calculated absorption coefficients of the SOAP at $\lambda = 400$, 550, 700 and 850 nm. Again, the data lie close to the 1:1 line, and hence, the calculations reproduce the measured values. The correlation is highest at $\lambda = 400$ nm ($r = 0.988$) and lowest at $\lambda = 850$ nm ($r = 0.930$). The 'weaker' correlation for the larger wavelengths can be explained again by the influence of a variable imaginary part of the complex refractive index of the fine mode as follows. In contrast to the smaller wavelengths, the absorption for the larger wavelengths is more affected by the fine mode particles. Particles from the coarse particle modes with lower imaginary parts for larger wavelengths have a lower contribution to the absorption.

Nevertheless, Fig. 7b shows that for larger absorption coefficients at $\lambda = 400$, 700 and 850 nm, the calculated and measured values deviate from the 1:1 line. For $\lambda = 400$ nm, the calculations underestimate the measurements, whereas for $\lambda = 700$ and 850 nm the calculations overestimate the measurements systematically. As illustrated by time series in Fig. 7a, the differences between calculations and measurements are higher during dust dominated periods (DOY 24.5–26.5 LT and DOY 28–34 LT) than in the period with low dust concentration (from DOY 34 LT on).

The reason for this result could be a slightly different spectral behaviour of the calculated absorption coefficient and hence the imaginary part of mineral dust. Therefore, the next section describes the retrieval of an optical equivalent imaginary part of the refractive index for mineral dust.

4.2. *Soot mass closure at dry conditions and retrieval of an optical equivalent imaginary part of mineral dust*

The goal of this section is to retrieve an imaginary part of the complex refractive index for mineral dust, based on the measured absorption coefficients and PNSDs.

An accurate retrieval starts with the following equations for the absorption coefficients of the PM_1 PSAP and PM_{10} PSAP:

$$\begin{aligned} \sigma_a^{PM_1 PSAP} &= vf_{dust,PM_1} \cdot \sigma_{a,dust} + \sigma_{a,soot}, \\ \sigma_a^{PM_{10} PSAP} &= \sigma_{a,dust} + \sigma_{a,soot}, \end{aligned} \tag{3}$$

where $\sigma_{a,dust}$ and $\sigma_{a,soot}$ are the absorption coefficients of dust and soot, respectively. vf_{dust,PM_1} is the volume fraction of dust within PM_1 and is illustrated in Fig. 8 for clarification. vf_{dust,PM_1} was calculated in analogy to eq. (2) and considers the sampling efficiency to the PSAP and the PM_1 penetration curve (eq. 1). The error for vf_{dust,PM_1} was estimated to 24%, since the largest uncertainty to determine vf_{dust,PM_1} (as well as vf_{dust}; see argumentation on this in Section 4.1.1) results from the determination of the number fraction of nearly hydrophobic dust particles. Subsequently, eq. (3) was rearranged yielding an equation for the

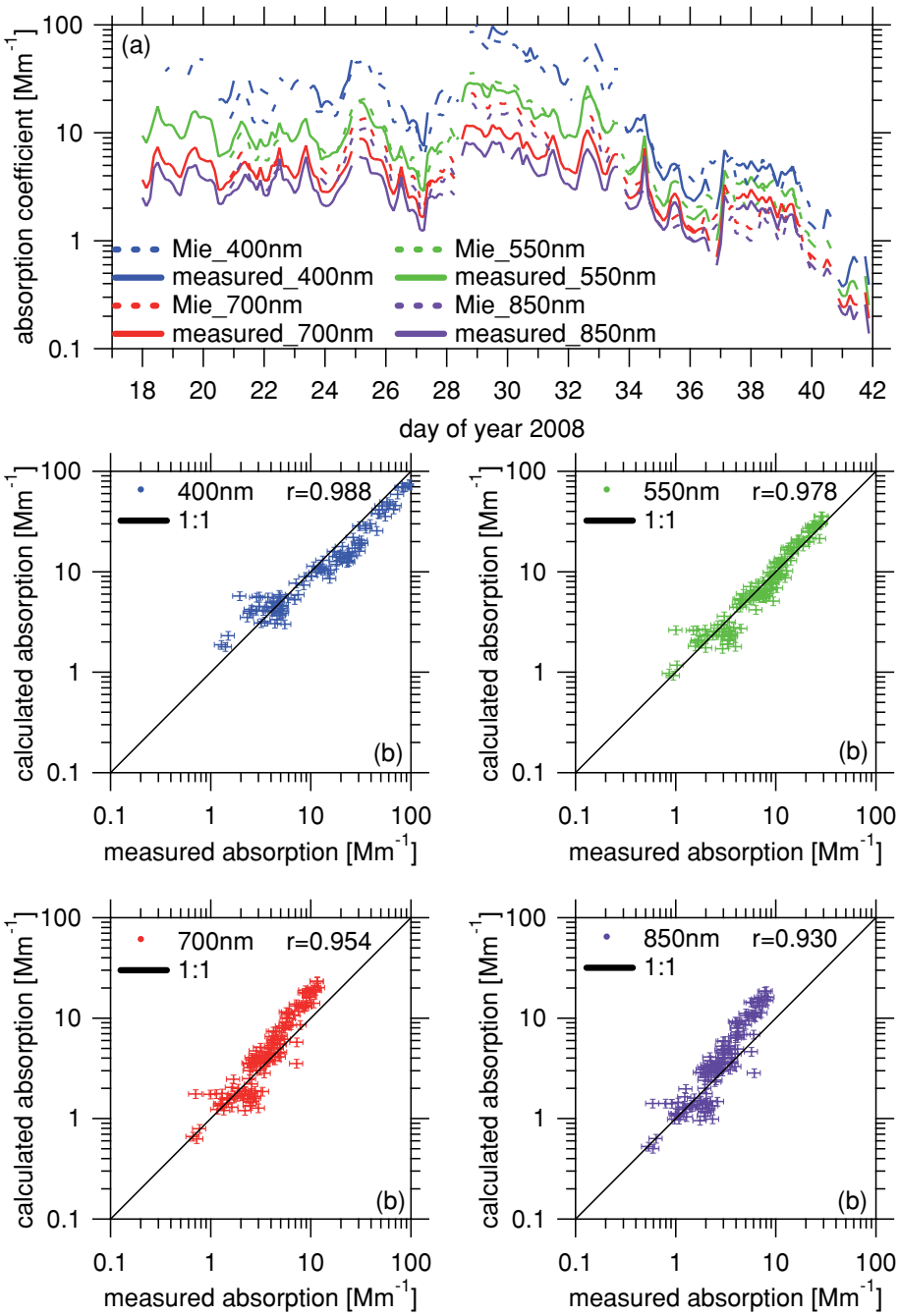

Fig. 7. (a) Time series of Mie calculated and measured absorption coefficients of the SOAP at $\lambda = 400$, 550, 700 and 850 nm. (b) Scatter plots of calculated and measured absorption coefficients at the four wavelengths. The error for the measured values is given by the SOAP uncertainty (15%), while the error for the calculated values (single standard deviation) is 10% (Wex et al., 2002).

absorption coefficient of soot

$$\sigma_{\mathrm{a,soot}} = \frac{\sigma_{\mathrm{a}}^{\mathrm{PM_1PSAP}} - v\mathrm{f}_{\mathrm{dust,PM_1}} \cdot \sigma_{\mathrm{a}}^{\mathrm{PM_{10}PSAP}}}{1 - v\mathrm{f}_{\mathrm{dust,PM_1}}}. \quad (4)$$

For validation, the retrieved absorption coefficient of soot was averaged within the time interval of the measured soot mass concentration from the RAMAN spectrometer. Figure 9 shows the result of the soot closure as a scatter plot. The mass absorption cross section (MAC) converts the absorption coefficient into a mass concentration and vice versa. Bond and Bergstrom (2006) reported MACs of soot ranging from 3 to 16 $m^2\ g^{-1}$ at $\lambda = 550$ nm including laboratory aerosol, diesel engines and

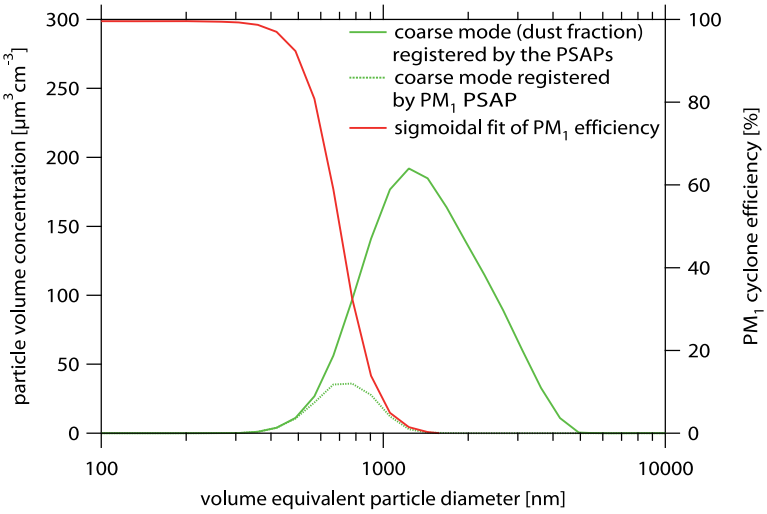

Fig. 8. Illustration of the dust volume concentration within PM_1 (green dotted line). The dotted line was derived by multiplying the sigmoidal fit of the PM_1 penetration curve (red solid line, equation 1) with the nearly hydrophobic (mineral dust) particle volume concentration of the coarse mode (green solid line).

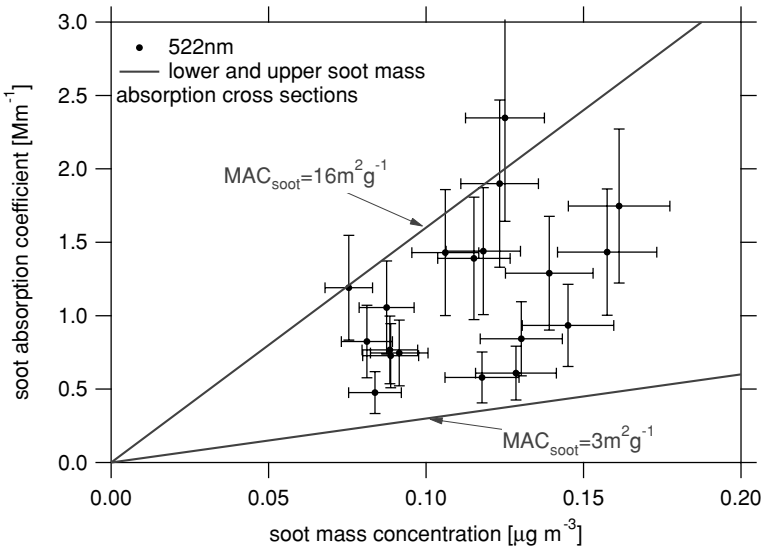

Fig. 9. Scatter plot of retrieved soot absorption coefficients versus measured soot mass concentration. The error for the soot mass concentration is given by the uncertainty of the Raman spectrometer (10%), while the error for the soot absorption coefficient is 30%.

carbon black. These lower and upper boundaries of MAC at $\lambda =$ 550 nm (wavelength is close to the PSAP wavelength) are added in Fig. 9 by straight lines. The uncertainty of the retrieved absorption coefficient of soot is ~30% and was estimated from the PSAP uncertainty (6%) and the uncertainty for vf_{dust,PM_1} (24%). Regarding this large uncertainty of ~30%, the soot mass closure was still successful since the data points were within the boundaries.

Finally, the spectral absorption coefficient of soot was calculated using an Ångström-absorption exponent of unity (Bergstrom et al., 2002; Kirchstetter et al., 2004). The spectral absorption coefficient of mineral dust was determined using the measured absorption coefficient by the SOAP (σ_a^{SOAP})

$$\sigma_{a,dust}(\lambda) = \sigma_a^{SOAP}(\lambda) - \sigma_{a,soot}(\lambda). \quad (5)$$

An optical equivalent imaginary part of the complex refractive index of mineral dust was retrieved with Mie calculations and the secant method. During the iteration, only the imaginary part was varied, while the real part of the complex refractive index was set to 1.53 (Table A1). The iteration was repeated until the Mie calculated (σ_a^{Mie}) and the measured spectral absorption coefficient of mineral dust fitted within a small residual $\varepsilon = \left(\frac{\sigma_a^{Mie} - \sigma_{a,dust}}{\sigma_{a,dust}}\right)^2 < 1.0{*}10^{-6}$ (cf. Cheng et al., 2006). Table 1 shows the arithmetic mean values of the optical equivalent imaginary part. For comparison, literature values for mineral dust imaginary parts from Hess et al. (1998) and Müller et al. (2009a) are added. As expected from the dry absorption optical closure (Section 4.1.2), the retrieved optical equivalent imaginary part are up to 80% higher (at $\lambda = 300$ nm) than in Hess et al. (1998) for $\lambda < 550$ nm. In contrast to that, the imaginary parts of this investigation are

Table 1. Literature values and arithmetic mean values from this investigation for the imaginary part of the refractive index for mineral dust. The data in the last column are arithmetic mean values from a time series containing a dust volume fraction of at least 90% and data of at least 55 of 66 wavelengths per time interval

Wavelength (nm)	Mineral dust imaginary part from Hess et al. (1998)	Mineral dust imaginary part from Müller et al. (2009a)	Mineral dust imaginary part from this investigation
300	$2.5 \cdot 10^{-2}$	$2.3 \cdot 10^{-2}$	$4.50 \cdot 10^{-2}$
350	$1.7 \cdot 10^{-2}$	$1.3 \cdot 10^{-2}$	$3.70 \cdot 10^{-2}$
400	$1.3 \cdot 10^{-2}$	$7.9 \cdot 10^{-2}$	$2.80 \cdot 10^{-2}$
450	$8.5 \cdot 10^{-3}$	$5.1 \cdot 10^{-2}$	$1.50 \cdot 10^{-2}$
500	$7.8 \cdot 10^{-3}$	$3.5 \cdot 10^{-2}$	$1.00 \cdot 10^{-2}$
550	$5.5 \cdot 10^{-3}$	$1.6 \cdot 10^{-2}$	$5.60 \cdot 10^{-3}$
600	$4.5 \cdot 10^{-3}$	$7.0 \cdot 10^{-4}$	$3.70 \cdot 10^{-3}$
650	$4.5 \cdot 10^{-3}$	$5.0 \cdot 10^{-4}$	$2.90 \cdot 10^{-3}$
700	$4.0 \cdot 10^{-3}$	$3.0 \cdot 10^{-4}$	$2.70 \cdot 10^{-3}$
750	$4.0 \cdot 10^{-3}$	$2.0 \cdot 10^{-4}$	$2.70 \cdot 10^{-3}$
800	$4.0 \cdot 10^{-3}$	$4.0 \cdot 10^{-4}$	$2.50 \cdot 10^{-3}$
900	$4.0 \cdot 10^{-3}$		$2.40 \cdot 10^{-3}$

up to 40% lower (at $\lambda = 900$ nm) for $\lambda > 550$ nm. Comparing the imaginary parts with values for pure Saharan mineral dust derived by Müller et al. (2009a) during SAMUM-1, the imaginary parts from this study are shifted to larger values. This may have several reasons.

A trajectory analysis (Knippertz et al., 2011) revealed a different origin of the Saharan dust registered at the sites of SAMUM-2 and SAMUM-1. Different chemical compounds of the Saharan dust may change the imaginary part of the refractive index. Another investigation by Kandler et al. (2011) points out that the volume fraction of iron oxides was slightly higher than during SAMUM-1.

Another reason might be aged soot particles, which accumulated on a mineral dust particle during transport, and causes an increase of the imaginary part of mineral dust. However, such a soot-dust mixture was rarely observed (Lieke et al., 2011).

In the following, to describe the optical properties of the fraction of nearly hydrophobic coarse mode particles, the derived optical equivalent imaginary part of the refractive index for mineral dust was used.

4.3. Numerical calculations of the influence of particle shape on AOPs at dry conditions and consequences for AOPs at humidified conditions

This section gives numerical calculations of non-spherical shaped mineral dust particles for AOPs. The influence of the particle shape of mineral dust on the scattering coefficient was quantified in Section 4.1.1. With this information and using the optical equivalent imaginary part to calculate the absorption coefficient, the influence of particle non-sphericity on the extinction coefficient can be computed via Mie-theory. The same method can be employed to calculate the influence of particle shape on the single scattering albedo ω_0.

Numerous research studies (Mishchenko et al., 1995; Mishchenko et al., 1997; Kalashnikova and Sokolik, 2002; Kalashnikova et al., 2005; Bi et al., 2010) gave numerical solutions of optical properties for arbitrarily shaped mineral dust particles. The results from these studies can however be only approximations of non-sphericity effects on AOPs for this study, since the used PNSD, complex refractive indices and equivalent particle diameters deviate. For this case, a database for (prolate) spheroids, deformed spheroids, and aggregates (Gasteiger et al., 2011) was used. The database includes the scattering matrix as well as the extinction and scattering efficiencies. Here, the particle diameter of the non-spherical particle is defined as the diameter of a sphere that has the same volume (dp_{ve}). To simulate the effect on optical properties of modeled non-spherical dust particles, the optical equivalent imaginary part given in Table 1 and the corresponding real parts of the complex refractive index (Table A1) were used. However, the database for the deformed spheroids and aggregates include imaginary parts only up to $3.44 \cdot 10^{-2}$. For this case, computations of these shapes were made only for wavelengths larger than 350 nm. The computations of the deformed spheroids and aggregates using discrete dipole approximation (DDA) are limited to a size parameter $x = \pi \frac{dp_{ve}}{\lambda} \approx 25$. Hence, to compare the DDA results with results made with TMM (T–Matrix method, spheroids) and the reference case (spheres), the upper particle diameter of the mineral dust PNSD was set to $dp_{ve} = 2650$ nm.

For the calculation of the scattering matrix of spheroids, a particle size-independent aspect ratio distribution was taken from Wiegner et al. (2009). The optical properties of the deformed spheroids were averaged for three aspect ratios (1.4, 1.8 and 2.4). The deformed spheroids are prolate spheroids with surface deformations according to the Gardner series, as described in Gasteiger et al. (2011). For aggregate particles, a single shape is considered only.

The non-sphericity factors of the extinction coefficient (scattering coefficient) range from 1.085 to 1.305 (1.094–1.363) at $\lambda = 450$ nm to 1.034–1.129 (1.035–1.133) at $\lambda = 880$ nm and are highest for the aggregates and lowest for the spheroids. From the present data it can be concluded, that the smoother the particle is the smaller is the non-sphericity factor. The extinction and the scattering non-sphericity factors show a wavelength dependency and the influence of non-spherical particle shape decreases with increasing wavelength. This wavelength dependency is in agreement with the scattering non-sphericity factors (see Fig. 5) and with other investigations (e.g. Koepke and Hess, 1988; Kalashnikova et al., 2005). The enhancement of the extinction by non-spherical particles at short wavelengths may be explained by the fact that the cross-section of a particle is the driving parameter for extinction, if particles are larger than the wavelength. For a given particle volume, the cross section of the particle and subsequently, the extinction increases with increasing non-sphericity of the particle.

Nevertheless, the aforementioned scattering and extinction non-sphericity factors are lower than the derived non-sphericity factors of mineral dust from this study (Fig. 5).

Lower non-sphericity factors for the spheroids, deformed spheroids, and aggregates were found for the single scattering albedo (1.00–1.044) and the asymmetry parameter (0.997–1.045). For the three shape classes, the non-sphericity factor of ω_0 shows a wavelength dependency and increases for smaller wavelengths. This property is basically caused by the stronger increase of the scattering non-sphericity factor compared to the extinction non-sphericity factor. The non-sphericity factor of the asymmetry parameter does not show such a characteristic pattern.

The measured non-sphericity factors of ω_0 of mineral dust from this investigation are almost larger than the values for the spheroids, deformed spheroids, and aggregates and range from 0.1% at $\lambda = 950$ nm over 4% at $\lambda = 550$ nm to 36% at $\lambda = 300$ nm. There are two reasons for that. The revealed scattering non-sphericity factor from this study is larger than the scattering non-sphericity factor of the three shapes classes. In addition, the influence of the scattering non-sphericity factor on the non-sphericity factor of ω_0 increases, the lower ω_0 is. This effect results from the particle non-sphericity and was also observed by Kalashnikova et al. (2005) comparing strongly absorbing dust (lower single scattering albedo) and weakly absorbing dust (higher single scattering albedo). To conclude, particle shape effects of mineral dust aerosol should be considered, for example, in model calculations for single scattering albedos <0.95. In case of $\omega_0 < 0.95$, calculations using spherical dust particles provide incorrect results. Müller et al. (2011) show shape-independent measurements of the single scattering albedo at the site.

Differences in AOPs due to the non-spherical particle shape of mineral dust at dry conditions lead to consequences for quantification of AOPs at humidified conditions. Due to the nearly hydrophobic behavior of the Saharan mineral dust at Cape Verde (Schladitz et al., 2011), we assume that the AOPs and hence the non-sphericity factors do not change during the humidification process. Therefore, the scattering non-sphericity factor for the mineral dust component in the coarse mode is also considered for aerosol model calculations at ambient conditions.

5. Aerosol model calculations at ambient conditions

The aim of the aerosol model is to calculate microphysical and optical properties at ambient conditions using the RH as the only input parameter. A Mie code was applied to calculate the optical properties.

The aerosol model describes the optical and microphysical properties of the marine and Saharan dust aerosol. The microphysical part of the aerosol model is described by time series of the lognormal size distribution, hygroscopicity parameters for the hygroscopic and nearly hydrophobic particles, and corresponding number fractions. The optical part in terms of the complex refractive index for each lognormal size distribution and mixing state is described by Tables A1 and 1. To describe the non-spherical shape of Saharan mineral dust particles, the wavelength-dependent non-sphericity factor for scattering (Fig. 5) is incorporated.

The first step to calculate the microphysical and optical properties at ambient conditions is to transform the dry PNSD being measured outside the measurement container as follows. During the aerosol transport from outside to the measurement systems, particle losses were calculated for the particle segregation through the PM_{10} inlet, the automatic aerosol dryer, the aerosol splitter, and connection tubes to the size spectrometer. Starting at the inlet, the penetration efficiency of a PM_{10} inlet with a flow rate of 18 l min^{-1} (close to the required flow rate of 16.7 l min^{-1}) is given by Liu et al. (1983) and Lee et al. (1986). The particle transmission efficiency through the aerosol dryer is taken from Tuch et al. (2009). The aerosol splitter splits the sample flow rate of the APS (1 l min^{-1}) from the inlet flow rate nearly isokinetically with minimal particle losses as seen in Fig. 10. Downstream of the aerosol splitter, the APS was connected by $2 \times 45^\circ$ bends and a tube of 0.5 m length with an inclination angle of about 30°. The product of all transmission efficiencies is the total transmission efficiency for the dry PNSD shown in Fig. 10.

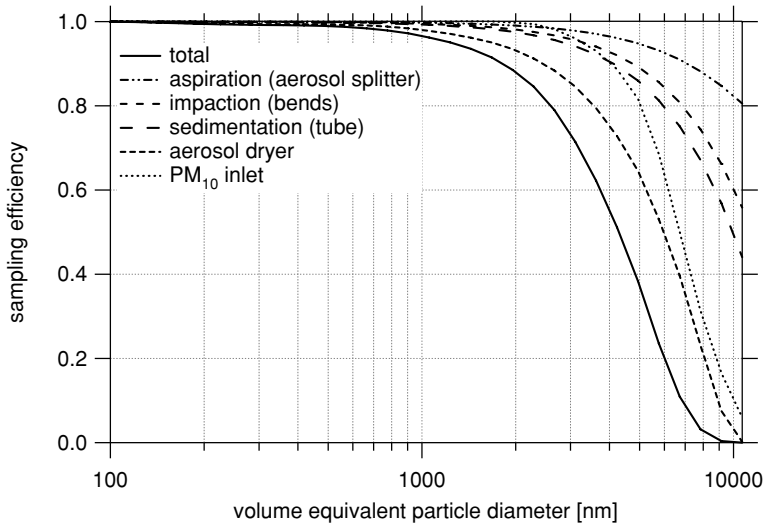

Fig. 10. Sampling efficiencies for the dry PNSD through particle transport losses in the sampling lines and particle segregation in the PM_{10} inlet.

The dry PNSD was divided by the total transmission efficiency up to a size of about $dp_{ve} = 7$ μm, yielding a dry PNSD, which was corrected for particle losses.

5.1. *Comparison of humidification factors at ambient conditions*

The aim of this section is to compare the enhancement of calculated and measured extinction coefficients due to hygroscopic growth at ambient conditions. The dry PNSD corrected for particle losses was transformed to ambient conditions. Therefore, each bin of the dry PNSD was multiplied with the time- and size-dependent number fractions of hygroscopic and nearly hydrophobic particles. The dry diameters of the hygroscopic and nearly hydrophobic PNSDs were multiplied bin-wise with the hygroscopic growth factors at ambient RH. The hygroscopic growth factors were iteratively calculated from the time- and size-dependent hygroscopicity parameters κ using eq. (11) in Petters and Kreidenweis (2007). To ensure conservation of the total particle number concentration, the number concentrations of the size bins of the PNSDs were modified according to the change of the size interval width.

The complex refractive index at the actual RH was calculated bin-wise using the Maxwell–Garnett relation (Maxwell-Garnett, 1904) and the mean hygroscopic growth factors as

$$\frac{\tilde{m}\,(\mathrm{RH})^2 - \tilde{m}^2}{\tilde{m}\,(\mathrm{RH})^2 + 2\tilde{m}^2} = \left(1 - \frac{1}{\mathrm{GF}^3}\right) \cdot \frac{\tilde{m}_\mathrm{w}^2 - \tilde{m}^2}{\tilde{m}_\mathrm{w}^2 + 2\tilde{m}^2}. \tag{6}$$

Here, $\tilde{m}$ represents the dry complex refractive index tabulated in Tables A1 and 1, $\tilde{m}(\mathrm{RH})$ is the complex refractive index at the actual RH, and $\tilde{m}_\mathrm{w}$ is the complex refractive index of water (Hale and Querry, 1973), whereas GF is the RH, size- and time-dependent hygroscopic growth factor.

The extinction coefficient σ_e calculated for container conditions ($T = 293$ K, $p = 1000$ hPa) was adjusted to the actual ambient temperature T_amb and atmospheric pressure p_amb using equation

$$\sigma_\mathrm{e}\,(T_\mathrm{amb}, p_\mathrm{amb}) = \sigma_\mathrm{e} \cdot \frac{293\ \mathrm{K}}{T_\mathrm{amb}} \frac{p_\mathrm{amb}}{1000\ \mathrm{hPa}}. \tag{7}$$

The extinction coefficient was measured at $p_\mathrm{amb} \approx 1000$ hPa (1.5 m above the container).

A direct comparison of extinction coefficients measured by the visibility sensor and calculated by the aerosol model is not possible, since the internally stored calibration constant (converts the measured receiver signal into an extinction coefficient) is only valid for foggy conditions and is unfortunately unknown. Therefore, data from the visibility sensor were used as a relative measurement of the extinction coefficient exemplified in the following. The ratio of measured extinction at ambient conditions to the calculated extinction was normalized to unity for cases, where no significant particle growth is expected (RH $<$ 40%). This ratio is called measured humidification factor for the extinction coefficient and is plotted in Fig. 11a. For comparison, the ratio of the calculated extinction coefficient at ambient conditions to the calculated extinction at dry conditions was determined. This ratio, which is called calculated humidification factor for the extinction coefficient as well as the measured ambient RH is added to Fig. 11a.

The aerosol model reproduces the measured humidification factor very well. Until DOY 34 LT, calculated and measured humidification factors are close to unity. However, from DOY 34 both curves show an increase for the humidification factors. This behaviour is caused by a lower dust fraction and thus a higher fraction of sea-salt particles. A higher fraction of hygroscopic sea-salt particles are grown up at RH between 40% and 80% and this may enhance the extinction significantly. Figure 11b shows a

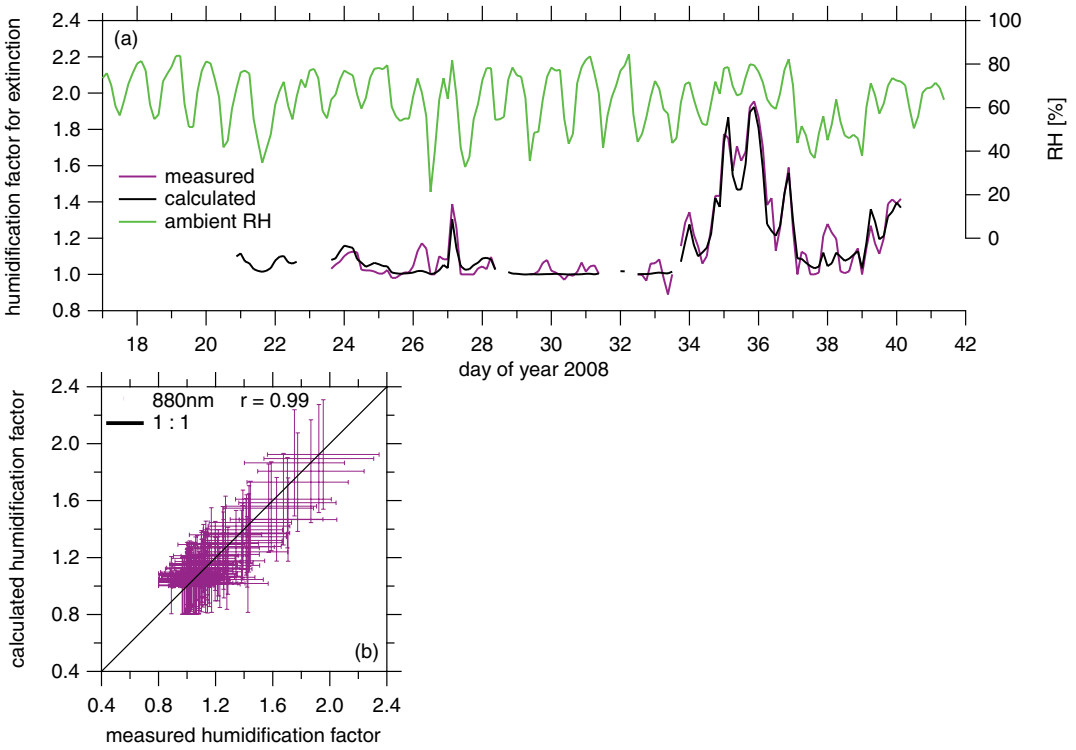

Fig. 11. (a) Time series of measured and calculated humidification factors for the extinction coefficient at ambient conditions. The upper panel shows also the registered RH on top of the measurement container. (b) Scatter plot of calculated versus measured humidification factors for the extinction coefficient. The error of the calculated humidification factor for the extinction coefficient was assumed to 20% regarding uncertainties in quantifying the sampling efficiency of the dry PNSD.

scatter plot of calculated versus measured humidification factors. Both values correlate very well ($r = 0.99$) and lie on the 1:1 line.

From this comparison, it was concluded that the aerosol model is able to simulate RH effects and thus hygroscopic growth effects on AOPs.

5.2. *Comparison of calculated extinction with lidar data*

This section proofs the applicability of the calculated extinction coefficient by the aerosol model in the atmospheric boundary layer. Vertical profiles of the extinction coefficient were measured with various lidar systems at the measurement site. Tesche et al. (2009) give an overview of the lidar systems. One of them, the MULIS lidar (Wiegner et al., 1995; Freudenthaler et al., 2009) has the advantage to measure columnar extinction and backscatter coefficients within the atmospheric boundary layer down to a height of $\sim$ 150 m above ground ($\sim$ 250 m above sea level at the measurement site). The extinction coefficients from this lidar system were compared with the calculated extinction at the ground. The lidar profiles of the particle extinction coefficients were analysed with the Fernald-algorithm (Fernald, 1984), using the lidar ratio derived from simultaneous Raman measurements. For further details concerning the data processing and the determination of measurement errors refer to Groß et al. (2011). In contrast to the lidar, the aerosol model wasn't developed to resolve the vertical structure of the extinction coefficient. In fact, the simulation of aerosol layers in the atmosphere is a challenge for aerosol transport models. Nevertheless, the validity of the calculated extinction coefficient at ambient conditions was tested using ground-based measurements (Schladitz et al., 2011). A vertical profile of meteorological parameters, for example, RH, atmospheric pressure, and temperature was provided by radiosonde (Vaisala RS80, RS92) launches at the site at least once a day. The RH was used to calculate the RH-dependent extinction coefficient. Employing equation 7, information on temperature and pressure shown in Figs 12a and 13a were used to adjust the calculated extinction from container to ambient conditions.

Figures 12b and 13b show average vertical lidar profiles of the extinction coefficient at $\lambda = 532$ nm from DOY 29.786 to 29.8375 LT and DOY 37.604 to 37.625 LT, respectively. These two lidar profiles were chosen, since the extinction coefficients were measured closest to the ground at all for a case of high dust concentrations and hence high extinction coefficients at the ground (Fig. 12) and a case of low dust concentrations (Fig. 13).

Calculations of extinction coefficients of the total aerosol were done twice, from scattering coefficients including spherical dust particles (without scattering non-sphericity factor) and

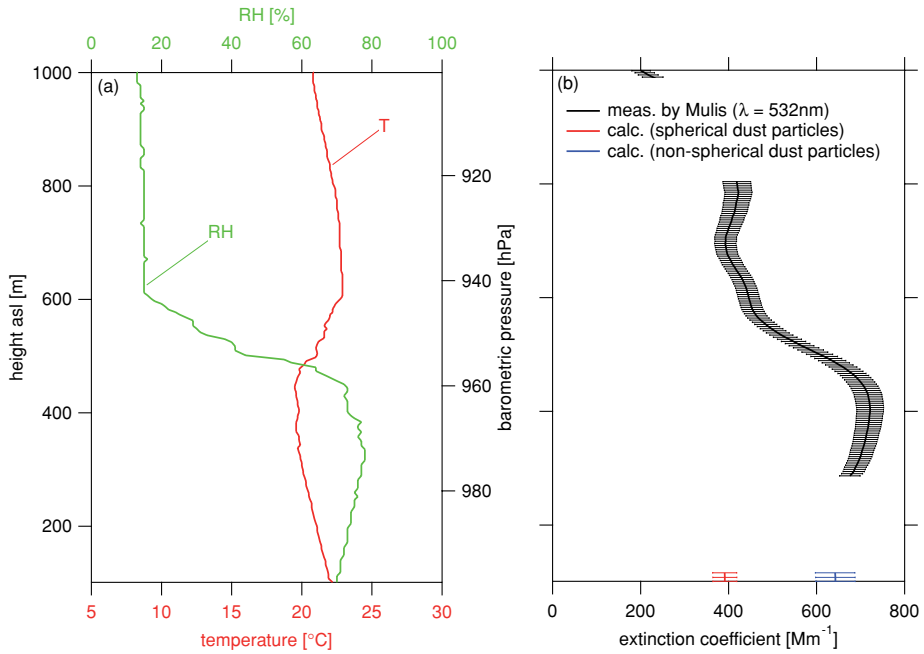

Fig. 12. (a) Relative humidity and temperature profiles up to 1000 m height at DOY 29.829 LT. (b) Measured (black solid line) and calculated (non-spherical dust particles: blue solid line, spherical dust particles: red solid line) extinction coefficients averaged from DOY 29.744–29.796 LT. The error for the measured values is given in Groß et al. (2011), while the error for the calculated values is 7%.

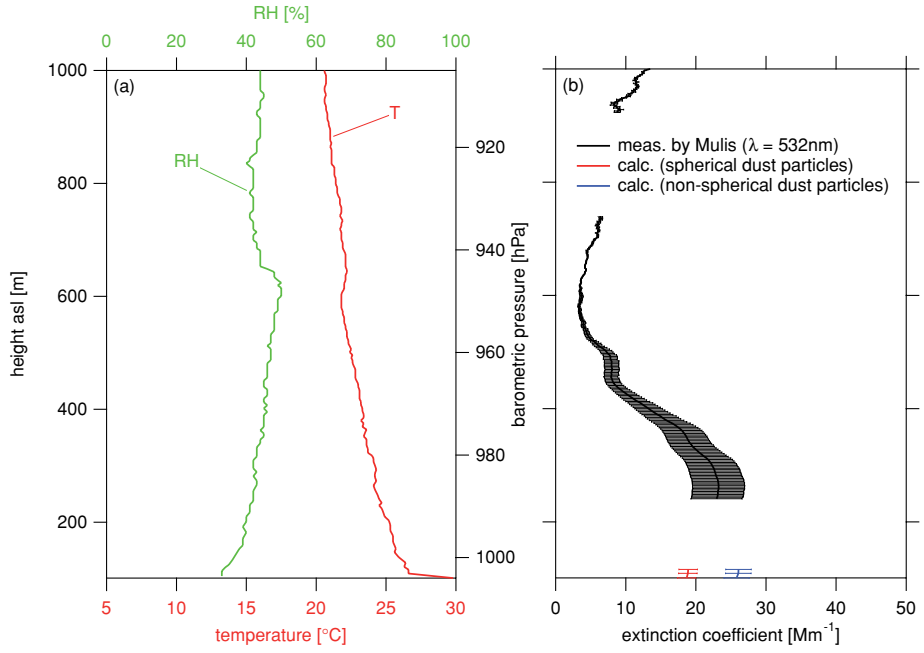

Fig. 13. (a) Same as Fig. 12a but for DOY 37.572 LT. (b) Same as Fig. 12b but for DOY 37.563–37.583 LT.

from scattering coefficients including non-spherical dust particles (with scattering non-sphericity factor). The calculated extinction coefficients for the lowest two points are shown in Figs. 12b and 13b for comparison. The humidity and temperature profiles in Fig. 12 indicate a shallow marine boundary layer (MBL) up to 400 m above sea level (asl). The adjacent temperature inversion and a decreasing RH indicate the Saharan dust layer. In the MBL, the measured extinction coefficient increases

up to 700 Mm^{-1}. The calculated extinction coefficients show large differences applying spherical and non-spherical dust particles. The measured extinction coefficient closest to the ground, agrees with the non-spherical approach (deviation of $6 \pm 11\%$), while the spherical model does not (deviation of $73 \pm 13\%$). The comparison at high dust concentrations clearly revealed that an assumption of spherical dust particles significantly underestimate the extinction coefficients.

In contrast to Fig. 12a, Fig. 13a indicates not such a clear layering in the radiosonde profiles. The profiles revealed only a small temperature inversion at about 650 m height asl, which marks the top of the MBL. As illustrated in fig. 1 in Knippertz et al. (2011), the adjacent upper aerosol layer is composed of a mixture of dust and smoke. In the MBL, the measured extinction coefficient increases up to 25 Mm^{-1}. For the lowermost layer, the spherical as well as the non-spherical calculations agree with the measured extinction profile (deviation of $17 \pm 29\%$ and $12 \pm 23\%$, respectively). This fact is not surprising, because the lower the ratio of the dust particle number concentration to the total particle number concentration is, the lower is the effect of non-sphericity of the extinction coefficient.

To summarize, both case studies revealed that on the one hand the aerosol model is not capable to reproduce the shape of the extinction profile in the MBL. On the other hand, the model can compensate missing extinction measurements near the ground. It is important to complete the profile from the ground to the uppermost layers, to compare integrated aerosol extinction with directly measured from the sun-photometer. In our case studies, the extinction coefficient is at highest in the lowermost layers. Disregarding of these not by lidar systems detectable layers may lead to systematic errors for such intercomparison studies.

6. Parametrization of humidity effects of optical aerosol properties

Time series of AOPs were calculated with the aerosol model at the dry state and at 55, 75 and 90% RH in the range from $\lambda =$ 300 to 950 nm with steps of 50 nm. The calculated AOPs are the scattering, absorption, and extinction coefficient as well as the asymmetry parameter and the single scattering albedo. As discussed above, the scattering coefficient of mineral dust particles shows significant differences between non-spherical and spherical particle shape. Therefore, calculations of the scattering coefficient for the nearly hydrophobic fraction of the coarse mode were made for spherical and non-spherical dust particles. Extinction coefficients for the nearly hydrophobic fraction of the coarse mode were calculated from the sum of the scattering coefficient (with and without scattering non-sphericity factor) and the absorption coefficient. Also the single scattering albedo of the total aerosol was calculated twice, from scattering and extinction coefficients including spherical dust particles and from scattering and extinction coefficients including non-spherical dust particles.

The RH dependence of AOPs can be described by the humidification factor

$$\xi_{\mathrm{AOP}}(\lambda, \mathrm{RH}) = \frac{\mathrm{AOP}(\lambda, \mathrm{RH})}{\mathrm{AOP}(\lambda, \mathrm{dry})}. \tag{8}$$

Here, AOP(dry) refers to RH $< 30\%$. This value is close enough to dry conditions, because it is supposed that further drying of the air does not change the AOP (Charlson et al., 1984). Humidification factors were calculated for the extinction coefficient ξ_{e}, the scattering coefficient ξ_{s}, the absorption coefficient ξ_{a}, the single scattering albedo $\xi_{\omega 0}$ and the asymmetry parameter ξ_g. An often used parametrization of ξ_{AOP} (e.g. in Kasten, 1969; Hänel, 1976; Hegg et al., 1996; Grant et al., 1999; Anderson et al., 2003; Carrico et al., 2003; Nessler et al., 2005; Quinn et al., 2005; Cheng et al., 2008) is based on a power law. The dependency of ξ_{AOP} is adopted from the power law characteristic of the metastable branch of the hysteresis of hygroscopic growth. The goal of this investigation is to find a simple parametrization of ξ_{AOP} for further use in radiative transfer models. The best fit for all AOPs was found by using equation

$$\xi_{\mathrm{AOP}}(\lambda, \mathrm{RH}) = \left(1 - \frac{\mathrm{RH}}{100}\right)^{\gamma(\lambda) \cdot \frac{\mathrm{RH}}{100}}, \tag{9}$$

where the free parameter $\gamma(\lambda)$ was derived using a non-linear least-squares routine (Levenberg–Marquardt method). This was done for ξ_{e}, ξ_{s}, ξ_{a}, ξ_{g}, while $\xi_{\omega 0}$ can be derived from ξ_{e} and ξ_{s} and the humidification factor for the single scattering albedo is given by

$$\xi_{\omega_0} = \frac{\xi_{\mathrm{s}}}{\xi_{\mathrm{e}}}. \tag{10}$$

Equation (9) equals eq. (5) in Cheng et al. (2008) for $\mathrm{RH}_0 =$ 0% and is valid in the range from 0 to 90% RH. In eq. (9), the power increases with increasing RH, accounting for the steeper behaviour of ξ_{AOP} at high RH. The advantage of this parametrization is that it describes the RH dependency of the power with no further parameter. For instance, Hänel (1984) used different power functions to parametrize the humidification factors for several RH ranges.

A general correlation of $\gamma(\lambda)$ and λ was not found, but Cheng et al. (2008) reported that the free parameter $\gamma(\lambda)$ depends on the chemical composition. Quinn et al. (2005) parametrize the γ value as a linear function of the relative amount of organic particulate matter for submicrometer aerosol. Another study by Howell et al. (2006) carried out during ACE-Asia reported that ξ_{s} depends on the dust volume fraction. On the basis of Howell et al. (2006), it was found to be adequate to parametrize $\gamma(\lambda)$ as a function of the dry dust volume fraction ($v\mathrm{f}_{\mathrm{dust}}$, eq. 2) by

$$\gamma(\lambda) = y_0(\lambda) + A(\lambda) \cdot (v\mathrm{f}_{\mathrm{dust}})^{\mathrm{pow}(\lambda)}. \tag{11}$$

For this study, three free parameters $y_0(\lambda)$, $A(\lambda)$ and $\mathrm{pow}(\lambda)$ were determined for each AOP by a non-linear least-squares fit. Tables 2–5 summarize the fit parameters $\pm$ single standard deviation for each AOP. For the extinction and scattering, the fit parameters

Table 2. Coefficients ± single standard deviation for the humidification factor of the extinction coefficient for spherical (sph) and non-spherical (nsp) dust particles

Wavelength (nm)	y_0 (sph)	y_0 (nsp)	A (sph)	A (nsp)	pow (sph)	pow (nsp)
300	-0.521 ± 0.026	-0.587 ± 0.055	0.483 ± 0.024	0.567 ± 0.053	3.145 ± 0.355	1.777 ± 0.273
350	-0.546 ± 0.029	-0.618 ± 0.061	0.512 ± 0.027	0.599 ± 0.059	2.932 ± 0.339	1.71 ± 0.273
400	-0.561 ± 0.031	-0.635 ± 0.065	0.533 ± 0.029	0.619 ± 0.062	2.792 ± 0.325	1.664 ± 0.27
450	-0.576 ± 0.033	-0.659 ± 0.07	0.552 ± 0.031	0.646 ± 0.068	2.669 ± 0.305	1.568 ± 0.259
500	-0.575 ± 0.034	-0.661 ± 0.073	0.555 ± 0.032	0.65 ± 0.071	2.535 ± 0.291	1.505 ± 0.254
550	-0.582 ± 0.035	-0.666 ± 0.074	0.566 ± 0.033	0.657 ± 0.071	2.457 ± 0.282	1.501 ± 0.251
600	-0.582 ± 0.037	-0.661 ± 0.072	0.568 ± 0.034	0.653 ± 0.07	2.364 ± 0.275	1.506 ± 0.25
650	-0.584 ± 0.039	-0.661 ± 0.073	0.572 ± 0.037	0.653 ± 0.071	2.234 ± 0.269	1.488 ± 0.249
700	-0.587 ± 0.041	-0.651 ± 0.069	0.576 ± 0.039	0.643 ± 0.067	2.181 ± 0.268	1.552 ± 0.252
750	-0.593 ± 0.044	-0.647 ± 0.068	0.583 ± 0.041	0.64 ± 0.066	2.096 ± 0.269	1.585 ± 0.256
800	-0.594 ± 0.047	-0.638 ± 0.067	0.585 ± 0.045	0.631 ± 0.064	2.003 ± 0.27	1.601 ± 0.261
850	-0.604 ± 0.052	-0.636 ± 0.066	0.595 ± 0.049	0.628 ± 0.064	1.953 ± 0.282	1.673 ± 0.275
900	-0.603 ± 0.052	-0.621 ± 0.06	0.596 ± 0.05	0.614 ± 0.058	1.908 ± 0.275	1.753 ± 0.272
950	-0.615 ± 0.055	-0.619 ± 0.056	0.609 ± 0.052	0.612 ± 0.054	1.891 ± 0.278	1.86 ± 0.277

Table 3. Coefficients ± single standard deviation for the humidification factor of the scattering coefficient for spherical (sph) and non-spherical (nsp) dust particles

Wavelength (nm)	y_0 (sph)	y_0 (nsp)	A (sph)	A (nsp)	pow (sph)	pow (nsp)
300	-0.529 ± 0.017	-0.576 ± 0.039	0.469 ± 0.017	0.55 ± 0.037	4.821 ± 0.475	2.284 ± 0.289
350	-0.55 ± 0.02	-0.602 ± 0.043	0.497 ± 0.019	0.578 ± 0.041	4.313 ± 0.431	2.194 ± 0.288
400	-0.564 ± 0.022	-0.619 ± 0.048	0.522 ± 0.021	0.599 ± 0.045	3.846 ± 0.386	2.077 ± 0.282
450	-0.583 ± 0.026	-0.65 ± 0.057	0.552 ± 0.024	0.635 ± 0.055	3.271 ± 0.331	1.825 ± 0.264
500	-0.583 ± 0.029	-0.655 ± 0.062	0.56 ± 0.027	0.644 ± 0.06	2.922 ± 0.303	1.689 ± 0.256
550	-0.593 ± 0.032	-0.668 ± 0.067	0.575 ± 0.03	0.659 ± 0.064	2.667 ± 0.284	1.608 ± 0.25
600	-0.593 ± 0.034	-0.667 ± 0.067	0.579 ± 0.032	0.658 ± 0.065	2.498 ± 0.272	1.579 ± 0.246
650	-0.594 ± 0.037	-0.667 ± 0.069	0.582 ± 0.034	0.659 ± 0.067	2.331 ± 0.264	1.545 ± 0.244
700	-0.596 ± 0.038	-0.657 ± 0.065	0.585 ± 0.036	0.65 ± 0.063	2.266 ± 0.261	1.605 ± 0.246
750	-0.601 ± 0.041	-0.654 ± 0.064	0.592 ± 0.039	0.647 ± 0.062	2.17 ± 0.261	1.635 ± 0.249
800	-0.601 ± 0.044	-0.644 ± 0.063	0.593 ± 0.042	0.637 ± 0.06	2.073 ± 0.261	1.662 ± 0.253
850	-0.609 ± 0.048	-0.64 ± 0.062	0.601 ± 0.046	0.633 ± 0.06	2.021 ± 0.273	1.729 ± 0.267
900	-0.608 ± 0.049	-0.625 ± 0.056	0.602 ± 0.046	0.619 ± 0.054	1.97 ± 0.266	1.807 ± 0.263
950	-0.62 ± 0.051	-0.623 ± 0.052	0.614 ± 0.049	0.617 ± 0.05	1.951 ± 0.269	1.919 ± 0.268

are added for spherical dust particles. In contrast to $\gamma(\lambda)$, the three fit parameters and the wavelength are clearly connected. For the extinction, scattering, and absorption y_0 decreases, and A increases with increasing wavelength. For the extinction and scattering, pow decreases with increasing wavelength.

In the special case $vf_{dust} = 0$, eq. (11) simplifies to $\gamma(\lambda) = y_0(\lambda)$ and means that the parameter $y_0(\lambda)$ represents the pure marine (background) aerosol. During the field campaign, vf_{dust} varied between 0.5 and 1.0. Strictly speaking, eq. (11) is valid in that range. To check the validity of this equation at $vf_{dust} = 0$, the humidification factors ξ_e, ξ_s, ξ_a, ξ_g and $\xi_{\omega 0}$ were calculated for the RH range from 0 to 90% and were compared with literature values.

In literature, humidification factors for specific aerosols, several AOPs and additionally for a wide range of RH are primarily based on model calculations. Directly measured humidification factors of AOPs are rare for marine aerosol. ξ_s was measured by Covert et al. (1972) and Anderson et al. (2003) using a combination of a humidified and a dry nephelometer. By using the same measurement technique, Hegg et al. (1996), Carrico et al. (1998), Kotchenruther et al. (1999) and Carrico et al. (2003) reported measured humidification factors for the scattering coefficient in the range from 2.0 to 2.5 at 80% RH. This value agrees with values from this investigation (Fig. 14).

The calculated humidification factors for pure marine aerosol were compared with modeled humidification factors from

Table 4. Coefficients ± single standard deviation for the humidification factor of the absorption coefficient

Wavelength (nm)	y_0	A	pow
300	-0.017 ± 0.006	0.017 ± 0.006	1 ± 0.483
350	-0.014 ± 0.005	0.013 ± 0.004	1 ± 0.449
400	-0.013 ± 0.004	0.013 ± 0.004	1 ± 0.472
450	-0.018 ± 0.006	0.018 ± 0.005	1 ± 0.415
500	-0.024 ± 0.007	0.024 ± 0.007	1 ± 0.404
550	-0.036 ± 0.011	0.035 ± 0.011	1 ± 0.407
600	-0.049 ± 0.014	0.047 ± 0.014	1 ± 0.391
650	-0.054 ± 0.012	0.051 ± 0.012	1.175 ± 0.392
700	-0.061 ± 0.015	0.059 ± 0.014	1.14 ± 0.392
750	-0.068 ± 0.016	0.065 ± 0.016	1.148 ± 0.39
800	-0.074 ± 0.019	0.071 ± 0.019	1.091 ± 0.391
850	-0.08 ± 0.023	0.077 ± 0.023	1 ± 0.397
900	-0.083 ± 0.022	0.08 ± 0.021	1.072 ± 0.393
950	-0.087 ± 0.024	0.083 ± 0.023	1.038 ± 0.393

Table 5. Coefficients ± single standard deviation for the humidification factor of the asymmetry parameter

Wavelength (nm)	y_0	A	pow
300	-0.073 ± 0.013	0.079 ± 0.013	1 ± 0.221
350	-0.084 ± 0.013	0.088 ± 0.012	1 ± 0.189
400	-0.079 ± 0.008	0.081 ± 0.008	1.343 ± 0.188
450	-0.059 ± 0.003	0.058 ± 0.003	2.587 ± 0.225
500	-0.064 ± 0.002	0.062 ± 0.002	2.856 ± 0.222
550	-0.054 ± 0.002	0.053 ± 0.002	3.173 ± 0.227
600	-0.062 ± 0.002	0.061 ± 0.002	3.367 ± 0.231
650	-0.054 ± 0.002	0.053 ± 0.002	3.115 ± 0.231
700	-0.06 ± 0.002	0.059 ± 0.002	3.173 ± 0.233
750	-0.049 ± 0.002	0.048 ± 0.002	2.936 ± 0.259
800	-0.058 ± 0.003	0.057 ± 0.003	2.895 ± 0.28
850	-0.052 ± 0.003	0.052 ± 0.003	2.981 ± 0.319
900	-0.052 ± 0.003	0.051 ± 0.003	2.723 ± 0.353
950	-0.057 ± 0.004	0.056 ± 0.003	2.856 ± 0.36

literature at 50, 70, 80 and 90% RH. First, the models are introduced, which are called 'maritime polluted' (OPAC, Hess et al., 1998), 'maritime-polluted' (D'Almeida et al., 1991), 'maritime model' (Shettle and Fenn, 1979) and 'maritime aerosol (model 3)' (Hänel, 1976).

In the OPAC model three different types of 'maritime' models are given. The 'maritime polluted' aerosol type was used for a validation, since it contains a soot lognormal size distribution.

The humidification factors from D'Almeida et al. (1991) are valid for polluted maritime environment in the Mediterranean and the north Atlantic and based on three lognormal size distributions. The 'maritime-polluted' aerosol comprises a water soluble, a soot and a sea-salt lognormal size distribution, respectively. The particle growth to equilibrium size at a distinct RH is based on Köhler theory, whereas the AOPs are calculated via Mie theory.

The humidification factors from Hänel (1976) are based on measured particle mass, mean particle density, and real part of the complex index of refraction at specific RH onboard the research vessel 'Meteor' in 1969 over the central Atlantic. The given AOPs (ξ_e, ξ_a and $\xi_{\omega 0}$ at $\lambda = 300$ and 550 nm) for the 'maritime aerosol (model 3)' are also calculated with Mie theory.

The 'maritime model' from Shettle and Fenn (1979) is composed of a so-called 'rural model' and a sea-salt component. The respective particle growth factors stem from Hänel (1976) from his 'model 6' and 'model 2'. The given AOPs (ξ_e, ξ_s, ξ_a, ξ_g and $\xi_{\omega 0}$ at $\lambda = 300$, 550 and 700 nm) are also calculated with Mie theory.

For ξ_e and ξ_s (Figs. 14a and b), the best agreement—in particular for a higher RH—is found for the 'maritime-polluted' aerosol from D'Almeida et al. (1991). The 'maritime polluted' model by Hess et al. (1998) shows the highest values at all. The values for ξ_a (Fig. 14c) lie between the 'maritime-polluted' aerosol and the 'maritime model', while the latter show $\xi_a < 1$. In contrast of this, for $\xi_{\omega 0}$ (Fig. 14d) the best agreement is found for the 'maritime model' by Shettle and Fenn (1979). For $\xi_{\omega 0}$, the 'maritime aerosol (model 3)' by Hänel (1976) shows the largest values at all. These large values are maybe caused by very low single scattering albedos in the visible spectral range around 0.7 at dry conditions. For ξ_g (Fig. 14e), the best agreement is again found for the 'maritime-polluted' aerosol.

To conclude, in literature, there are still differences between humidification factors of one aerosol type. The humidification factors for pure marine aerosol from this study agree within the variability of literature values. Therefore, it is reasonable to extend the validity of the parametrization (eq. 11) from $v\mathrm{f}_{\mathrm{dust}} = 0$ to 1.

7. Summary and conclusion

There is a gap of understanding the humidity effects of AOPs of mixed aerosol species, which also treats the non-sphericity of particles. The present work is a comprehensive investigation for RH effects on AOPs for the two most important natural aerosol sources (marine and Saharan dust aerosol). The AOPs include the extinction, scattering, and absorption coefficient as well as the single scattering albedo and the asymmetry parameter.

This work is based on measurements of microphysical properties (PNSDs, hygroscopic growth factors and the hygroscopic mixing state) and optical properties (dry scattering and absorption coefficients and ambient extinction coefficient) conducted at Praia, Cape Verde in the frame of SAMUM-2. An aerosol model was developed to describe these properties for the marine and Saharan dust aerosol. Microphysical parameters are delivered by Schladitz et al. (2011). Parameters for optical properties

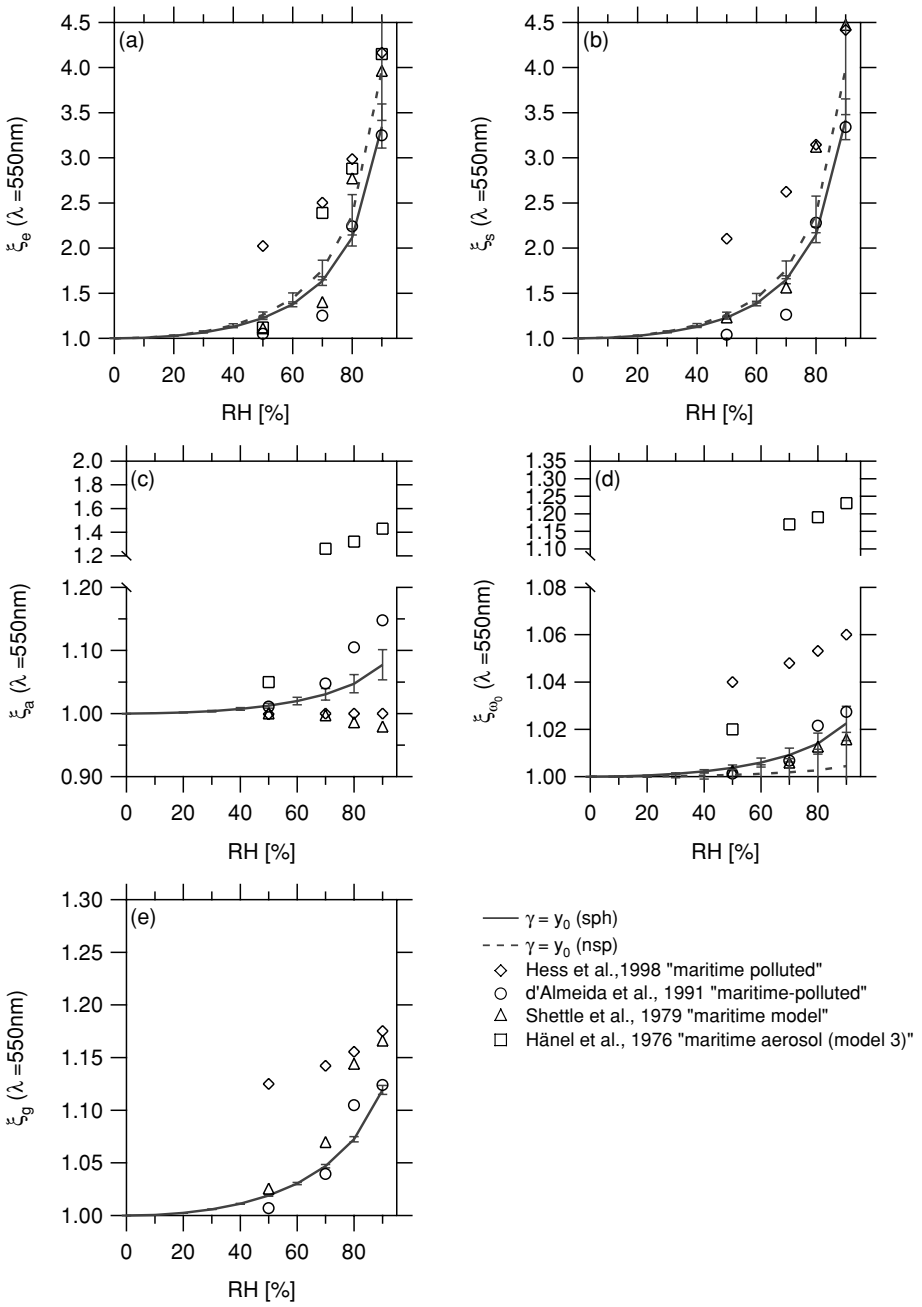

Fig. 14. Comparison of humidification factors for the (a) extinction, (b) scattering, and (c) absorption coefficient as well as (d) single scattering albedo and (e) asymmetry parameter for the marine aerosol. Humidification factors from this investigation calculated using spherical dust particles (grey solid line) and non-spherical dust particles (grey dashed line) and the corresponding error bars result from the standard deviation of y_0. Additionally, humidification factors are added from Hess et al. (1998) (open diamonds), D'Almeida et al. (1991) (open circles), Shettle and Fenn (1979) (open triangles) and Hänel (1976) (open squares).

in terms of complex refractive index were taken from literature. The aerosol model was validated with measured scattering and absorption coefficients at dry conditions and with a relative measure of the extinction coefficient at ambient conditions. Within an optical closure at dry conditions, a wavelength-dependent scattering non-sphericity factor for mineral dust was derived. To investigate the influence of the non-sphericity on the AOPs, the scattering non-sphericity factor is incorporated in the aerosol model. The optical equivalent imaginary part of the complex refractive index of Saharan mineral dust was derived from a

comparison of measured and calculated absorption coefficients. At this stage, the aerosol model was adapted to the measured optical properties at dry conditions.

For ambient conditions, the calculated and measured humidification factors of the extinction coefficient fit with a Pearson's correlation coefficient of almost unity. With this intercomparison, it was demonstrated that the aerosol model is able to quantify the humidity effect of AOPs. This study also reveals the importance of hygroscopic growth of large sea-salt particles for any RH below 90%.

The aerosol model was applied to calculate the extinction coefficients in the lowermost layers of the atmosphere and to show that it might be possible to extend the measured lidar profiles to the ground when non-spherical dust particles are taken into account. With this completed lidar profile from the ground to the uppermost aerosol layers, the integrated aerosol extinction, for example, the aerosol optical depth can be used to validate satellite products and can be compared to sun-photometer data.

Parametrizations of humidification factors were derived in the wavelength range from $\lambda = 300$ to 950 nm, to quantify the enhancement of AOPs at a distinct RH from 0 to 90% and for a dry dust volume fraction between 0 and 1. Following the common literature to describe optical properties at ambient conditions, the humidification factors were parametrized by a power law. From this power law, a time series of a parameter γ was derived, which is solely dependent on the aerosol optical property and wavelength. γ shows a dependence on the dry dust volume fraction and was parametrized by three parameters using a power law formalism. The parametrization was extended to describe the humidity dependence of optical properties of the clean marine aerosol. The humidification factors from the parametrization agreed within the literature values of the marine aerosol.

The parametrization derived in this investigation can be implemented in radiative transfer calculations to consider the humidity dependence of AOPs from the dry state up to 90% RH for regions of pure Saharan dust, regions with influence of marine and Saharan dust, and regions of pure marine aerosol. However, the parametrization is only valid for particles being in a metastable equilibrium with the surrounding moist air. Beyond that, current radiative transfer models are mainly based on Mie calculations. It was shown that under certain conditions, for example, high dust concentrations, the Mie approach delivers incorrect AOPs, which would result to incorrect radiative transfer calculations.

In summary, this study presents two equations to calculate the humidity dependence of AOPs of a mixture of Saharan dust and marine aerosol. With known RH, wavelength, and dry dust volume fraction, the humidity dependence of AOPs can be calculated from three tabulated parameters, which depend on the wavelength and the aerosol optical property.

8. Acknowledgements

This study was supported by the German Research Foundation under grant FOR 539 in the framework of the research group SAMUM. We acknowledge Mr. Konrad Kandler, who provides us meteorological data. Finally, we thank the two anonymous reviewers for their useful comments.

9. Appendix

Table A1. Complex refractive indices from the OPAC database (Hess et al., 1998) for the different particle modes and hygroscopic mixing state. For the coarse mode, the complex refractive index for 'sea-salt (0% RH)' was assigned to the hygroscopic particles, while 'mineral' was assigned to the nearly hydrophobic particles. The complex refractive index for the fine mode was calculated by using an internal mixture of 8% 'soot' and 92% 'insoluble' for the nearly hydrophobic particles, and 8% 'soot' and 92% 'water soluble (0% RH)' for the hygroscopic particles

Wavelength (nm)	Coarse (nearly hydrophobic)	Coarse (hygroscopic)	Fine (nearly hydrophobic)	Fine (hygroscopic)
300	$1.53–2.5 \cdot 10^{-2}i$	$1.51–2.00 \cdot 10^{-6}i$	$1.55–4.50 \cdot 10^{-2}i$	$1.55–4.50 \cdot 10^{-2}i$
350	$1.53–1.7 \cdot 10^{-2}i$	$1.51–3.24 \cdot 10^{-7}i$	$1.55–4.46 \cdot 10^{-2}i$	$1.55–4.48 \cdot 10^{-2}i$
400	$1.53–1.3 \cdot 10^{-2}i$	$1.50–3.00 \cdot 10^{-8}i$	$1.55–4.42 \cdot 10^{-2}i$	$1.55–4.14 \cdot 10^{-2}i$
450	$1.53–8.5 \cdot 10^{-3}i$	$1.50–2.43 \cdot 10^{-8}i$	$1.55–4.38 \cdot 10^{-2}i$	$1.55–4.10 \cdot 10^{-2}i$
500	$1.53–7.8 \cdot 10^{-3}i$	$1.50–1.55 \cdot 10^{-8}i$	$1.55–4.34 \cdot 10^{-2}i$	$1.55–4.06 \cdot 10^{-2}i$
550	$1.53–5.5 \cdot 10^{-3}i$	$1.50–1.00 \cdot 10^{-8}i$	$1.55–4.26 \cdot 10^{-2}i$	$1.55–4.07 \cdot 10^{-2}i$
600	$1.53–4.5 \cdot 10^{-3}i$	$1.49–1.60 \cdot 10^{-8}i$	$1.55–4.22 \cdot 10^{-2}i$	$1.55–4.03 \cdot 10^{-2}i$
650	$1.53–4.5 \cdot 10^{-3}i$	$1.49–4.24 \cdot 10^{-8}i$	$1.55–4.22 \cdot 10^{-2}i$	$1.55–4.12 \cdot 10^{-2}i$
700	$1.53–4.0 \cdot 10^{-3}i$	$1.49–2.00 \cdot 10^{-7}i$	$1.55–4.18 \cdot 10^{-2}i$	$1.55–4.08 \cdot 10^{-2}i$
750	$1.53–4.0 \cdot 10^{-3}i$	$1.49–1.08 \cdot 10^{-6}i$	$1.55–4.18 \cdot 10^{-2}i$	$1.55–4.22 \cdot 10^{-2}i$
800	$1.53–4.0 \cdot 10^{-3}i$	$1.48–1.95 \cdot 10^{-6}i$	$1.54–4.18 \cdot 10^{-2}i$	$1.54–4.36 \cdot 10^{-2}i$
900	$1.53–4.0 \cdot 10^{-3}i$	$1.48–4.24 \cdot 10^{-5}i$	$1.54–4.22 \cdot 10^{-2}i$	$1.54–4.68 \cdot 10^{-2}i$

References

Anderson, T. L., Covert, D. S., Marshall, S. F., Laucks, M. L., Charlson, R. J. and co-authors. 1996. Performance characteristics of a high-sensitivity, three-wavelength, total scatter/backscatter nephelometer. *J. Atmos. Oceanic Technol.* **13**, 967–986.

Anderson, T. L., Masonis, S. J., Covert, D. S., Ahlquist, N. C., Howell, S. G. and co-authors. 2003. Variability of aerosol optical properties derived from in situ aircraft measurements during ACE-Asia. *J. Geophys. Res.* **108**, 8647.

Anderson, T. L. and Ogren, J. A. 1998. Determining Aerosol radiative properties using the TSI 3563 integrating nephelometer. *Aerosol Sci. Technol.* **29**, 57–69.

Andreae, M. O. 1995. Climatic effects of changing atmospheric aerosol levels. In: *Future Climates of the World: A Modelling Perspective* (ed. A. Henderson-Sellers). Elsevier, Amsterdam, 347–398.

Andreae, M. O. and Gelencsér, A. 2006. Black carbon or brown carbon? The nature of light-absorbing carbonaceous aerosols. *Atmos. Chem. Phys.* **6**, 3131–3148.

Ansmann, A., Petzold, A., Kandler, K., Tegen, I., Wendisch, M. and co-authors. 2011. Saharan Mineral Dust Experiments SAMUM-1 and SAMUM-2: what have we learned? *Tellus* **63B**, this issue.

Bergstrom, R. W., Russell, P. B. and Hignett, P. 2002. Wavelength dependence of the absorption of black carbon particles: predictions and results from the TARFOX experiment and implications for the aerosol single scattering albedo. *J. Atmos. Sci.* **59**, 567–577.

Bi, L., Yang, P., Kattawar, G. W. and Kahn, R. 2010. Modeling optical properties of mineral aerosol particles by using nonsymmetric hexahedra. *Appl. Opt.* **49**, 334–342.

Bohren, C. F. and Huffman, D. R. 1983. *Absorption and Scattering of Light by Small Particles*. New York, John Wiley & Sons, Inc.

Bond, T. C., Anderson, T. L. and Campbell, D. 1999. Calibration and intercomparison of filter-based measurements of visible light absorption by aerosols. *Aerosol Sci. Technol.* **30**, 582–600.

Bond, T. C. and Bergstrom, R. W. 2006. Light Absorption by carbonaceous particles: an investigative review. *Aerosol Sci. Technol.* **40**, 27–67.

Bond, T. C., Covert, D. S. and Müller, T. 2009. Truncation and angular-scattering corrections for absorbing aerosol in the TSI 3563 nephelometer. *Aerosol Sci. Technol.* **43**, 866–871.

Brockmann, J. E. 1993. Sampling and transport of aerosols. In: *Aerosol Measurement—Principles, Techniques, and Applications* (eds K. Willeke and P. A. Baron). Van Nostrand Reinhold, New York, 77–108.

Carrico, C. M., Kus, P., Rood, M. J., Quinn, P. K. and Bates, T. S. 2003. Mixtures of pollution, dust, sea salt, and volcanic aerosol during ACE-Asia: radiative properties as a function of relative humidity. *J. Geophys. Res.* **108**, 8650.

Carrico, C. M., Rood, M. J. and Ogren, J. A. 1998. Aerosol light scattering properties at Cape Grim, Tasmania, during the First Aerosol Characterization Experiment (ACE 1). *J. Geophys. Res.* **103**, 16565–16574.

Carrico, C. M., Rood, M. J., Ogren, J. A., Neusüß, C., Wiedensohler, A. and Heintzenberg, J. 2000. Aerosol Optical properties at Sagres, Portugal during ACE 2. *Tellus* **52B**, 694–715.

Charlson, R. J., Covert, D. S. and Larson, T. B. 1984. Observation of the effect of humidity on light scattering by aerosols. In: *Hygroscopic Aerosols* (eds. L. H. Ruhnke and A. Deepak). A. Deepak, Hampton, VA, 35–44.

Cheng, Y. F., Eichler, H., Wiedensohler, A., Heintzenberg, J., Zhang, Y. H. and co-authors. 2006. Mixing state of elemental carbon and non-light-absorbing aerosol components derived from in situ particle optical properties at Xinken in Pearl River Delta of China. *J. Geophys. Res.* **111**, D20204.

Cheng, Y. F., Wiedensohler, A., Eichler, H., Heintzenberg, J., Tesche, M. and co-authors. 2008. Relative humidity dependence of aerosol optical properties and direct radiative forcing in the surface boundary layer at Xinken in Pearl River Delta of China: an observation based numerical study. *Atmos. Environ.* **42**, 6373–6397.

Chiapello, I., Bergametti, G., Chatenet, B., Bousquet, P., Dulac, F. and co-authors. 1997. Origins of African dust transported over the north-eastern tropical Atlantic. *J. Geophys. Res.* **102**, 13701–13709.

Covert, D. S., Charlson, R. J. and Ahlquist, N. C. 1972. A study of the relationship of chemical composition and humidity to light scattering by aerosols. *J. Appl. Meteor.* **11**, 968–976.

D'Almeida, G. A., Koepke, P. and Shettle, E. P. 1991. *Atmospheric Aerosols: Global Climatology and Radiative Characteristics*. Hampton, VA, Deepak.

Fernald, F. G. 1984. Analysis of atmospheric lidar observations: some comments. *Appl. Opt.* **23**, 652–653.

Forster, P., Ramaswamy, V., Artaxo, P., Berntsen, T., Betts, R. and co-authors. 2007. Changes in atmospheric constituents and in radiative forcing. In: *Climate Change 2007: The Physical Science Basis. Contribution of Working Group I to the Fourth Assessment Report of the Intergovernmental Panel on Climate Change* (eds S. Solomon, D. Qin, M. Manning, Z. Chen, M. Marquis, K. B. Averyt, M. Tignor and H. L. Miller). Cambridge University Press, Cambridge, United Kingdom and New York, USA.

Freudenthaler, V., Esselborn, M., Wiegner, M., Heese, B., Tesche, M. and co-authors. 2009. Depolarization ratio profiling at several wavelengths in pure Saharan dust during SAMUM 2006. *Tellus* **61B**, 165–179.

Gassó, S., Hegg, D. A., Covert, D. S., Collins, D., Noone, K. J. and co-authors. 2000. Influence of humidity on the aerosol scattering coefficient and its effect on the upwelling radiance during ACE-2. *Tellus* **52B**, 546–567.

Gasteiger, J., Wiegner, M., Toledano, C., Groß, S., Freudenthaler, V. and co-authors. 2011. Modeling lidar-relevant optical properties of complex mineral dust aerosols. *Tellus* **63B**, this issue.

Grant, K. E., Chuang, C. C., Grossman, A. S. and Penner, J. E. 1999. Modeling the spectral optical properties of ammonium sulfate and biomass burning aerosols: parameterization of relative humidity effects and model results. *Atmos. Environ.* **33**, 2603–2620.

Groß, S., Gasteiger, J., Freudenthaler, V., Wiegner, M., Geiß, A. and co-authors. 2011. Characterization of the planetary boundary layer during SAMUM-2 by means of lidar measurements. *Tellus* **63B**, this issue.

Hale, G. M. and Querry, M. R. 1973. Optical constants of water in the 200-nm to 200-μm wavelength region. *Appl. Opt.* **12**, 555–563.

Hänel, G. 1976. The properties of atmospheric aerosol particles as functions of the relative humidity at thermodynamic equilibrium with the surrounding moist air. *Adv. Geophys.* **19**, 74–189.

Hänel, G. 1984. Parameterization of the influence of relative humidity on optical aerosol properties. In: *Aerosols and Their Climatic Effects* (eds H. E. Gerber and A. Deepak). A. Deepak, Hampton, VA, 117–122.

Hegg, D. A., Covert, D. S., Rood, M. J. and Hobbs, P. V. 1996. Measurements of aerosol optical properties in marine air. *J. Geophys. Res.* **101**, 12893–12903.

Heintzenberg, J., Wiedensohler, A., Tuch, T. M., Covert, D. S., Sheridan, P. and co-authors. 2006. Intercomparisons and aerosol calibrations of 12 commercial integrating nephelometers of three manufacturers. *J. Atmos. Oceanic Technol.* **23**, 902–914.

Hess, M., Koepke, P. and Schult, I. 1998. Optical properties of aerosols and clouds: the software package OPAC. *Bull. Am. Meteorol. Soc.* **79**, 831–844.

Howell, S. G., Clarke, A. D., Shinozuka, Y., Kapustin, V. N., McNaughton, C. S. and co-authors. 2006. Influence of relative humidity upon pollution and dust during ACE-Asia: size distributions and implications for optical properties. *J. Geophys. Res.* **111**, D06205.

IPCC 2007. *Climate Change 2007: The Physical Science Basis. Contributions of Working Group I to the Fourth Assessment Report of the Intergovernmental Panel on Climate Change*. Cambridge, United Kingdom and New York, USA, Cambridge University Press.

Kalashnikova, O. V., Kahn, R., Sokolik, I. N. and Li, W. H. 2005. Ability of multiangle remote sensing observations to identify and distinguish mineral dust types: optical models and retrievals of optically thick plumes. *J. Geophys. Res.* **110**, D18S14.

Kalashnikova, O. V. and Sokolik, I. N. 2002. Importance of shapes and compositions of wind-blown dust particles for remote sensing at solar wavelengths. *Geophys. Res. Lett.* **29**, 38–31–38–34.

Kandler, K., Lieke, K., Benker, N., Emmel, C., Küpper, M. and co-authors. 2011. Electron microscopy of particles collected at Praia, Cape Verde, during the Saharan Mineral Dust Experiment: particle chemistry, shape, mixing state and complex refractive index. *Tellus* **63B**, this issue.

Kasten, F. 1969. Visibility forecast in the phase of pre-condensation. *Tellus* **21**, 631–635.

Kenny, L. C. and Gussman, R. A. 1997. Characterization and modelling of a family of cyclone aerosol preseparators. *J. Aerosol Sci.* **28**, 677–688.

Kenny, L. C. and Gussman, R. A. 2000. A direct approach to the design of cyclones for aerosol-monitoring applications. *J. Aerosol Sci.* **31**, 1407–1420.

Kirchstetter, T. W., Novakov, T. and Hobbs, P. V. 2004. Evidence that the spectral dependence of light absorption by aerosols is affected by organic carbon. *J. Geophys. Res.* **109**, D21208.

Knippertz, P., Tesche, M., Heinold, B., Kandler, K., Toledano, C. and Esselborn, M. 2011. Dust mobilization and aerosol transport from West Africa to Cape Verde: a meteorological overview of SAMUM-2. *Tellus* **63B**, this issue.

Koepke, P. and Hess, M. 1988. Scattering functions of tropospheric aerosols: the effects of nonspherical particles. *Appl. Opt.* **27**, 2422–2430.

Köhler, H. 1936. The nucleus in and the growth of hygroscopic droplets. *Trans. Faraday Soc.* **32**, 1152–1161.

Kotchenruther, R. A., Hobbs, P. V. and Hegg, D. A. 1999. Humidification factors for atmospheric aerosols off the mid-Atlantic coast of the United States. *J. Geophys. Res.* **104**, 2239–2251.

Lack, D. A., Quinn, P., Massoli, P., Bates, T., Coffman, D. and co-authors. 2009. Relative humidity dependence of light absorption by mineral dust after long-range atmospheric transport from the Sahara. *Geophys. Res. Lett.* **36**, L24805.

Lee, S. D., Schneider, T., Grant, L. D. and Verkerk, J. P. 1986. Aerosols: research, risk assessment and control strategies. In: *Proceedings of the II. U.S.-Dutch International Symposium on Aerosols*, Williamsburg, Va.

Li-Jones, X., Maring, H. B. and Prospero, J. M. 1998. Effect of relative humidity on light scattering by mineral dust aerosol as measured in the marine boundary layer over the tropical Atlantic Ocean. *J. Geophys. Res.* **103**, 31113–31121.

Lieke, K., Kandler, K., Scheuvens, D., Emmel, C., von Glahn, C. and co-authors. 2011. Particle chemical properties in the vertical column based on aircraft observations in the vicinity of Cape Verde Islands. *Tellus* **63B**, this issue.

Liu, B. Y. H., Pui, D. Y. H., Wang, X. Q. and Lewis, C. W. 1983. Sampling of carbon fiber aerosols. *Aerosol Sci. Technol.* **2**, 499–511.

Maxwell-Garnett, J. C. 1904. Colours in metal glasses and metal films. *Phils. Trans. Roy. Soc. Lond.* **203**, 385–420.

Mertes, S., Dippel, B. and Schwarzenböck, A. 2004. Quantification of graphitic carbon in atmospheric aerosol particles by Raman spectroscopy and first application for the determination of mass absorption effciencies. *J. Aerosol Sci.* **35**, 347–361.

Mishchenko, M. I., Lacis, A. A., Carlson, B. E. and Travis, L. D. 1995. Nonsphericity of dust-like tropospheric aerosols: implications for aerosol remote sensing and climate modeling. *Geophys. Res. Lett.* **22**, 1077–1080.

Mishchenko, M. I., Travis, L. D., Kahn, R. A. and West, R. A. 1997. Modeling phase functions for dustlike tropospheric aerosols using a shape mixture of randomly oriented polydisperse spheroids. *J. Geophys. Res.* **102**, 16831–16847.

Müller, T., Henzing, J. S., De Leeuw, G., Wiedensohler, A., Alastuey, A. and co-authors. 2010. Characterization and intercomparison of aerosol absorption photometers: result of two intercomparison workshops. *Atmos. Meas. Tech. Discuss.* **3**, 1511–1582.

Müller, T., Nowak, A., Wiedensohler, A., Sheridan, P., Laborde, M. and co-authors. 2009b. Angular illumination and truncation of three different integrating nephelometers: implications for empirical, size-based corrections. *Aerosol Sci. Technol.* **43**, 581–586.

Müller, T., Schladitz, A., Kandler, K. and Wiedensohler, A. 2011. Spectral particle absorption coefficients, single scattering albedos, and imaginary parts of refractive indices from ground based in-situ measurements at Cape Verde Island during SAMUM-2. *Tellus* **63B**, this issue.

Müller, T., Schladitz, A., Massling, A., Kaaden, N., Kandler, K. and co-authors. 2009a. Spectral absorption coefficients and imaginary parts of refractive indices of Saharan dust during SAMUM-1. *Tellus* **61B**, 79–95.

Nessler, R., Weingartner, E. and Baltensperger, U. 2005. Adaptation of Dry Nephelometer Measurements to Ambient Conditions at the Jungfraujoch. *Environ. Sci. Technol.* **39**, 2219–2228.

Petters, M. D. and Kreidenweis, S. M. 2007. A single parameter representation of hygroscopic growth and cloud condensation nucleus activity. *Atmos. Chem. Phys.* **7**, 1961–1971.

Quinn, P. K., Bates, T. S., Baynard, T., Clarke, A. D., Onasch, T. B., Wang, W. and co-authors. 2005. Impact of particulate organic matter on the relative humidity dependence of light scattering: a simplified parameterization. *Geophys. Res. Lett.* **32**, L22809.

Ramaswamy, V., Boucher, O., Haigh, J., Hauglustaine, D., Haywood, J. and co-authors. 2001. Radiative forcing of climate change. In:

Climate Change 2001: The scientific Basis. Contribution of Working Group I to the Third Assessment Report of the Intergovernmental Panel on Climate Change (eds J. T. Houghton, Y. Ding, D. J. Griggs, M. Noguer, P. J. van der Linden and D. Xiasu). Cambridge University Press, Cambridge, United Kingdom and New York, USA, 349–416.

Rosen, H., Hansen, A. D. A., Gundel, L. and Novakov, T. 1978. Identification of the optically absorbing component in urban aerosols. *Appl. Opt.* **17**, 3859–3861.

Schladitz, A., Müller, T., Kaaden, N., Massling, A., Kandler, K. and co-authors. 2009. In situ measurements of optical properties at Tinfou (Morocco) during the Saharan Mineral Dust Experiment SAMUM 2006. *Tellus* **61B**, 64–78.

Schladitz, A., Müller, T., Nowak, A., Kandler, K., Lieke, K., Massling, A. and Wiedensohler, A. 2011. In-situ aerosol characterization at Cape Verde. Part 1: particle number size distributions, hygroscopic growth, and state of mixing of the marine and Saharan dust aerosol. *Tellus* **63B**, this issue.

Seinfeld, J. H. and Pandis, N. S. 2006. *Atmospheric Chemistry and Physics: From Air Pollution to Climate Change*. Hoboken, NJ, John Wiley & Sons, Inc.

Shettle, E. P. and Fenn, R. W. 1979. Models for the aerosols of the lower atmosphere and the effects of humidity variations on their optical properties. *AFGL-TR-79–0214* Environmental Research Papers No. 675, 94 pp.

Tegen, I., Lacis, A. A. and Fung, I. 1996. The influence on climate forcing of mineral aerosols from disturbed soils. *Nature* **380**, 419–422.

Tesche, M., Ansmann, A., Müller, D., Althausen, D., Engelmann, R. and co-authors. 2009. Vertically resolved separation of dust and smoke over Cape Verde using multiwavelength Raman and polarization lidars during Saharan Mineral Dust Experiment 2008. *J. Geophys. Res.* **114**, D13202.

Tuch, T. M., Haudek, A., Müller, T., Nowak, A., Wex, H. and co-authors. 2009. Design and performance of an automatic regenerating adsorption aerosol dryer for continuous operation at monitoring sites. *Atmos. Meas. Tech.* **2**, 417–422.

Tuinstra, F. and Koenig, J. L. 1970. Raman spectrum of graphite. *J. Chem. Phys.* **53**, 1126–1130.

Wex, H., Neusüß, C., Wendisch, M., Stratmann, F., Koziar, C. and co-authors. 2002. Particle scattering, backscattering, and absorption coefficients: an in situ closure and sensitivity study. *J. Geophys. Res.* **107**, 8122.

Wiegner, M., Gasteiger, J., Kandler, K., Weinzierl, B., Rasp, K. and co-authors. 2009. Numerical simulations of optical properties of Saharan dust aerosols with emphasis on lidar applications. *Tellus* **61B**, 180–194.

Wiegner, M., Quenzel, H., Rabus, D., Volker, W., Volger, P. and co-authors. 1995. Mobile three-wavelength backscatter lidar of the Meteorological Institute of the University of Munich. In: *Proceedings of the Lidar and Atmospheric Sensing*, Munich, Germany.

Winklmayr, W., Wang, H. C. and John, W. 1990. Adaptation of the Twomey Algorithm to the Inversion of Cascade Impactor Data. *Aerosol Sci. Technol.* **13**, 322–331.

Yoon, S. C. and Kim, J. 2006. Influences of relative humidity on aerosol optical properties and aerosol radiative forcing during ACE-Asia. *Atmos. Environ.* **40**, 4328–4338.